

DETECTION AND QUANTIFICATION OF BACTERIAL SPECIES AND MAMMALIAN
CELLS ON A SMARTPHONE PLATFORM USING FLUORESCENCE IMAGING

by

Babak Safavinia

Copyright © Babak Safavinia 2022

A Thesis Submitted to the Faculty of the

DEPARTMENT OF BIOMEDICAL ENGINEERING

In Partial Fulfillment of the Requirements

For the Degree of

MASTER OF SCIENCE

In the Graduate College

THE UNIVERSITY OF ARIZONA

2022

THE UNIVERSITY OF ARIZONA
GRADUATE COLLEGE

As members of the Master's Committee, we certify that we have read the thesis prepared by *Babak Safavinia*, titled *Fluorescence Imaging of Bacterial Species and Mammalian Cells on a Smartphone Platform* and recommend that it be accepted as fulfilling the dissertation requirement for the Master's Degree.

Jeong-Yeol Yoon

Jeong-Yeol Yoon, PhD

Date: May 10, 2022

Minkyu Kim

Minkyu Kim, PhD

Date: May 10, 2022

Youngwook Won

Youngwook Won, PhD

Date: May 10, 2022

Final approval and acceptance of this thesis is contingent upon the candidate's submission of the final copies of the thesis to the Graduate College.

I hereby certify that I have read this thesis prepared under my direction and recommend that it be accepted as fulfilling the Master's requirement.

Jeong-Yeol Yoon

Jeong-Yeol Yoon, PhD

Master's Thesis Committee Chair

Biomedical Engineering

Date: May 10, 2022

ARIZONA

ACKNOWLEDGEMENTS

Firstly, I would like to thank Dr. Jeong-Yeol Yoon, my graduate advisor and principal investigator for his support and encouragement through the years; all his advice and guidance will stay with me. I would like to express my gratitude to Dr. Kaveh Laksari who gave me the opportunity to be part of his team as an undergraduate and get exposed to academic research. I'd also like to thank my committee members for their time and contribution: Dr. Minkyu Kim and Dr. Young-Wook Won.

Next, I would like to acknowledge the Math Department, especially Michelle Woodward and Blake Hamrick, for allowing me to continue being a teaching assistant in my graduate career.

I am grateful for my graduate mentors through the years: Dr. Alexander Day, Ryan Zenhausern, and Dr. Tiffany Ulep for being patient with me while I learned the ways of researching. I am also appreciative to my current Biosensors Lab members for always sharing their knowledge and giving me words of encouragement. And lastly, to all my friends, I am forever thankful for always being there for me.

DEDICATION

To my parents and my brother who showed me unconditional love and support throughout my life, I would not have been in the position I am if it weren't for you.

TABLE OF CONTENTS

LIST OF TABLES 7

LIST OF FIGURES 8

ABSTRACT..... 11

INTRODUCTION 13

 Clinical Need 13

 Current Technology 14

 Microbiological culturing 15

 Natural Killer cell culture 15

 Bacteria culture 16

 Smartphone Platform and Imaging Procedure 16

 Fluorescence microscope for quantifying NK Cell subpopulation 16

 Set-up for Identification of Bacteria presence 17

 Image analysis..... 18

 Machine Learning for Cell Chromatography Lane 18

 Autofluorescence Intensity Analysis 19

 Overview of thesis 19

 Future directions 21

 References..... 23

APPENDIX A: NATURAL KILLER CELL DETECTION, QUANTIFICATION, AND SUBPOPULATION IDENTIFICATION ON PAPER MICROFLUIDIC CELL CHROMATOGRAPHY USING SMARTPHONE-BASED MACHINE LEARNING CLASSIFICATION..... 27

 Abstract..... 28

 Introduction..... 29

 Materials and Methods..... 34

 Cell Culture and Confirmation of Surface Expression 34

 Particle Conjugation and Specificity Analysis..... 35

 Paper Microfluidic Chip Design, Fabrication, and Assay Procedure 36

 Design and Optimization of Smartphone Fluorescence Microscope 38

 Microscopic Image Analysis and Machine Learning Model for Cell Chromatography Lane 39

 Video Analysis and Data Extraction for the Flow Lane 43

 Results and Discussion 45

 Confirmation of Differential Particle Binding to IL-2 and NK-92 Cells..... 45

 Flow Profile Measurements from Smartphone Videos 47

 Cell Separation Validation on Chromatography Lane 49

Cell Chromatography with Benchtop Microscope.....	51
Cell Chromatography with Smartphone-Based Fluorescence Microscopy	52
Conclusions.....	55
Acknowledgements.....	56
References.....	57
Supplementary	62
APPENDIX B: SMARTPHONE-BASED AUTOFLUORESCENCE IMAGING TO DETECT BACTERIAL SPECIES ON LABORATORY SURFACES	73
Abstract.....	74
Introduction.....	75
Materials and methods	78
Bacteria culture	78
Imaging procedure	80
Experiments without LB.....	81
Image analysis.....	82
Results and discussion	84
Bacteria species with LB imaged on microscope slides	84
Bacteria species with LB imaged on laboratory desks.....	86
Selection of controls	88
Bacteria species resuspended in DI water imaged on laboratory desk	88
Experiments with a commercial UV flashlight.....	92
Conclusions.....	94
References.....	96

LIST OF TABLES

Table A-S1. All benchtop machine learning data.

Table A-S2. All smartphone machine learning data.

LIST OF FIGURES

Figure A-1. Paper microfluidic chip layout and assay procedure. Buffy coat blood sample is pipette-added to the single-channel cell chromatography lane in the right (A) and the fourchannel flow lane in a circular layout in the left (B). A smartphone fluorescence microscope captures the fluorescence microscopic images from a cell chromatography lane (A). Anti-CD56 conjugated fluorescence nanoparticles are used and binding of anti-CD56 particles slows down the movement of NK cells through paper pores (A). Anti-IL-2 and anti-CD56 conjugated nanoparticles are used and a smartphone captures the video of such flow and the flow profile is obtained (B). Cell chromatography images and flow data are fed into analysis codes and outputs results for machine learning classification (A) and flow rate (B).

Figure A-2. Image analysis/database generation pipeline. A) multiple benchtop or smartphone microscope images are taken sequentially starting from the sample input and moving outward at regular intervals. B) Microscope images are analyzed to extract out relevant data from each image, thus associating each image with multiple data points. C) The extracted data represents a cell chromatography profile, which is generated for each chip and has multiple dimensions of data. D) This data is saved to a database, along with the known CD56^{dim} ratio, to allow for machine learning model generation after the database has been completed.

Figure A-3. Confirmation of antibody conjugated particles' binding to IL-2 and NK-92 cells. A) Anti-IL-2 conjugated particles show the increased number of particle aggregates with increased IL-2 concentration and a representative microscope image where the red circles indicate locations where particles were found to have aggregated. Error bars represent standard error with $n = 3$. B) Anti-CD56 conjugated particles bind to two different subpopulations (CD56^{dim} and CD56^{bright}) of NK-92 cells, with different binding extents to each subpopulation.

Figure A-4. Flow profile measurements. A) Representative d (flow distance, mm) vs. t (time, s) plots for assaying IL-2. All raw plots are available in Supplementary Figure S1. B) Average K vs. IL-2 (target cytokine; solid line) and IL-6 (for cross-reactive experiments; dashed line) concentration (IU/mL) plot ($n = 3$). Error bars represent standard errors. * represents a significant difference from non-cytokine-spiked buffy coat samples ($p < 0.05$). Dashed line represents K values C) Representative d vs. t plots for assaying NK-92 cells. All raw plots are available in Supplementary Figure S2. D) Average K vs. NK-92 cell concentration (cells/mL) plot ($n = 3$). Error bars represent standard errors. * represents significant difference from non-cytokine-spiked buffy coat samples ($p < 0.05$).

Figure A-5. Cell chromatography principle. The schematic diagram (A) of the cell chromatography lane of the microfluidic chip in which cell subpopulations are separated along the chip length via capillary flow, augmented by the effect of particle binding. Example cell chromatography profiles for samples containing CD56^{dim}:CD56^{bright} ratios of 60:40 (B) and 100:0 (C) can be seen, representing how samples with a larger proportion of CD56^{dim} cells tend to have higher fluorescent profiles further down the chip due to the principle seen in (A).

Figure A-6. Machine learning cell chromatography results on both microscope platforms. A) Schematic representation of the smartphone-based fluorescence microscope image system used for cell chromatography in expanded CAD view. B) Image of smartphone microscope housing with example image displayed. C) Confusion matrix from the final smartphone microscope-based model, indicating a model accuracy of 89%. Whole data set is available in Supplementary Table S2. Processed fluorescence images are summarized in Supplementary Figure S4. D) Confusion matrix from the final benchtop microscope-based model, indicating a model accuracy of 89%. Whole data set is available in Supplementary Table S1.

Figure A-S1. d (flow distance, mm) vs. t (time, s) plots for assaying IL-2. Black lines indicate NTC, purple indicates 50 IU/mL IL-2, green indicates 100 IU/mL, blue indicates 15 IU/mL, orange indicates 200 IU/mL, and red indicates 250 IU/mL.

Figure A-S2. d (flow distance, mm) vs. t (time, s) plots for assaying NK-92. Black lines indicate NTC, grey indicates 102 NK cells/mL, blue indicates 103 NK cells/mL, and red indicates 104 NK cells/mL.

Figure A-S3. Optimization of drying time and LED angle

Figure A-S4. Adjusted smartphone fluorescence microscope images.

Figure A-S5: Confusion matrix depicting 4-class classification using the platform described in this study

Fig B-1. Bacteria autofluorescence imaging set up on a laboratory desk. Acrylic film (as a low-cost optical bandpass filter) is placed in front of the Samsung S20 camera to isolate the autofluorescence signal. A 405 nm LED is used to excite the bacteria droplet from the side. 10 μ L bacterial droplets are added on a microscope slide (shown in the figure) or directly on a laboratory desk surface.

Figure B-2: Smartphone images (raw and green channel) of the bacteria droplets with vs. without an acrylic filter. Clearer fluorescence can be observed with an acrylic filter.

Figure B-3. Box and whisker plots of average intensities for bacteria droplets (suspended in LB and diluted in DI water) placed on microscope slides. Example images of *E. coli* droplets at various concentrations are shown in the top. Bottom shows the box and whisker plots of *E. coli*, *S. Typhimurium*, and *S. aureus* droplets at various concentrations (all in CFU/cm²). Negative control (NC) on each plot is a dilution of three orders of magnitude of LB.

Figure B-4. Box and whisker plots of average intensities for bacteria droplets (suspended in LB and diluted in DI water) placed on laboratory desks. Example images of *E. coli* droplets at various concentrations are shown in the top. Bottom shows the box and whisker plots of *E. coli*, *S. Typhimurium*, and *S. aureus* droplets at various concentrations (all in CFU/cm²). Negative control (NC) on each plot is a dilution of three orders of magnitude of LB.

Figure B-5. Box and whisker plot of the average intensities of each bacteria species, *E. coli*, *S. Typhimurium*, and *S. aureus*, at the concentrations of 10⁵, 10⁴, and 10³ CFU/cm². LB was removed from bacterial samples. A smartphone, a 405 nm LED, an acrylic film, and green channel images were used. The controls of tap water (0.8-1.2 ppm), DI water, NaCl solution (1 µg/mL), and BSA solution (1 µg/mL) are also plotted. These control concentrations are equivalent to 10 mg/cm², approximating the LOD of bacteria, 10⁴ CFU/cm².

Figure B-6. Experiments were repeated with a commercial UV flashlight instead of a 405 nm LED. Blue channel images were used. All other conditions are identical to those shown in Fig. 5.

ABSTRACT

Current methods to detect and quantify biological samples, specifically Natural killer cells, *E. Coli*, *S. Typhimurium*, and *S. aureus*, require expensive and specialized equipment, trained personnel, and have a long time-to-result. The aims of this research are to reduce cost, decrease time of detection, and simplify current systems. Two platforms were developed that utilizes fluorescence analysis and a smartphone camera for imaging.

Natural killer cell subpopulations, CD56^{bright} and CD56^{dim}, are believed to have a correlation with the overall patient health and immune function. The first platform consists of paper microfluidic chip and a smartphone-based device to identify and quantify NK cell subpopulation. A droplet of buffy coat sample consisting of NK cells are placed onto a single flow lane unit in order to perform special separation of CD56^{bright} and CD56^{dim} cells. Anti-CD56 fluorescent nanoparticles are used as biomarkers due to differential bindings to NK cell subpopulations. A smartphone platform that utilizes a smartphone microscope, 473 nm LED, and a acrylic film to as an optical bandpass filter. The analysis is done using a cloud-based machine learning predictive modeling analyzed NK cell subpopulation differentiation. Cell subpopulation analysis showed 89% accuracy.

For the second platform, a smartphone platform was used to detect bacteria presence on laboratory surfaces. Three bacteria species that are commonly found on surfaces *E. Coli*, *S. Typhimurium*, and *S. aureus*, were investigated in this study. The current methods to detect bacteria requires culturing or staining. Autofluorescence from the bacteria was obtained using a 405 nm LED as a light source to excite and cause emission and an acrylic film was used again as an optical bandpass filter. ImageJ was used to analyze the images and quantify the fluorescent

intensity signals. The platform was able to detect the presence of all three bacteria species with a limit of detect of 10^4 CFU/ cm² and differentiate the species from controls.

INTRODUCTION

Clinical Need

Cancer is a disease in which the patient's cells grow uncontrollably and cell division is dysregulated. Tumor microenvironment is one of the main obstacles in cancer treatment due to its composition. It is composed of a mixture of cells that increase the cellular density which results in physical drug resistance [1]. NK Cells are an essential part of the immune since they are responsible for cytotoxic activities [2], which makes the identification and quantification of NK cells crucial making it the first biomarker investigated.

NK cells can be subdivided into subgroups based on their surface expressions of CD56^{bright} and CD56^{dim}. CD56^{bright} cells are immature CD56^{dim} cells and they are responsible for cytokine signaling, whereas, CD56^{dim} cells are the matured cells that are responsible for the cytotoxic killing [3]. The ratio of CD56^{bright} to CD56^{dim} cells is believed to correlate to the overall patient health [4], [5]. In our study, fluorescent particles were used to bind to the NK cells to allow for its detection and quantification.

Various types of bacterial species are frequently being experimented with in clinical and laboratory settings which increases the chance of bacterial contamination[6]. The presence of bacteria may influence clinical diagnoses and laboratory experiments which brings about the need to detect bacterial species on surfaces with a low cost and time of detection. Intrinsic fluorescence (autofluorescence) signals from bacterial species allow for the detection without the use of fluorescence staining. Autofluorescence can be generated from bacterial cell contents such as proteins, lipofuscins, nucleic acids, and porphyrins [7]–[9].

Escherichia coli (*E. Coli*) was found to be one of the major bacterial species in laboratory settings and exhibiting strong attachment to abiotic surfaces [10]. In addition, it has been reported that *Staphylococcus aureus* can survive well on many different surfaces as well [11]. It is important to differentiate bacterial species from other fluorescing controls on surfaces, therefore, *E. Coli*, *S. aureus*, and *Salmonella enterica* (including serovar Typhimurium) make up the second biomarker group of interest.

Current Technology

Currently, in order to accurately quantify NK cell subpopulations, the gold standard technique is using flow cytometry[12], [13]. In this method, a biological sample containing NK cells is passed through the system which separates and isolates the droplets and a light source emits light through each isolated droplet. The detector picks up the scattered light and based on the signal, the cellular contents of the cell can be extracted. Fluorescence activated cell sorting is also used in this system. In this case, various fluorophores are added to the biological samples containing NK cells and when passed through the system, the cells are separated based on their fluorescent signals [14]. The limitation of this method is the slow detection time, expensive equipment, and the need for highly trained personnel.

In the case of bacteria on surfaces, there are different methods used: culturing a sample, polymerase chain reaction (PCR), and antibody-based biosensors. The traditional method has been swabbing a sample of the bacteria off the surface, dissolving them into a solution, and culturing them on selective or differential media culture plates. Bacterial colonies are counted visually to identify and quantify the concentration. The drawback of this method is the long time-to-result since the sample has to be cultured overnight. PCR has also been used for rapid

detection. However, it requires specialized equipment such as a thermal cycler and gel electrophoresis system and highly trained personnel to extract the gene and operate such equipment [15]. Lastly, antibody-based biosensors, typically incorporated on paper strips or microfluidic devices, have also popularly been investigated for bacterial detection [16]. However, the system is not highly accurate and it still requires swab-sampling and manual loading onto the platforms. All of the above methods require sampling, manual sampling loading, and material preparations (media, PCR kits, antibodies, etc.).

Consequently, there exists a clear need in clinical diagnostic testing environments for cheaper, simpler, and rapid techniques. The goal of this thesis is to present methods and platforms that have been proven to identify and quantify biological samples, NK cells and bacterial species. These methods eliminate the need for highly trained personnel since the methods are simpler and easier to use.

Microbiological culturing

Natural Killer cell culture

In order to experiment with NK-92 cells, the cells have to be cultured and subcultured to obtain the subpopulations needed. To create the ideal culture media for the contact independent NK cells (NK92), TheraPeak X-Vivo-15 media was supplemented with 10% fetal bovine serum, 250 IU/ mL of interleukin-2, and 1% Penicillin. Cells were cultured at 37° C and 5% CO₂ in an incubator and the media was changed for the subpopulation type accordingly. For the NK-92 CD56^{bright} subpopulation in which cell concentration was determined via a hemocytometer, cells formed a pellet by centrifugation at 1500 RPM for 5 min and resuspended in fresh media at 500,000 cells/mL every three days. To produce the NK-92 CD56^{dim} subpopulation, cells had to be “exhausted” and were maintained in a media by extending the subculture time to 6 days. Cell

concentration was determined via a hemocytometer and additional media was added to the flask to maintain cells at a concentration of 500,000 cells/ mL.

Bacteria culture

As mentioned above, the three bacteria species that were used in the experiment were *E. Coli*, *S. Typhimurium*, and *S. aureus*. The culture media was made by adding 25g of lysogeny broth (LB) powder to 1 L of Deionized (DI) water and shaken until the powder was dissolved. The mixture was then placed into an autoclave at 20 psi and 270° C for 20 minutes; once completed the LB was ready to be used as culture media for all species. Next, 1 µg of *E. Coli* (in powder form) was added to a 15mL falcon tube and followed by 10 mL of LB. The falcon tube was sealed using parafilm and placed into an incubator at 37° C for 24 hours. The same procedure was followed for *S. Typhimurium* and *S. aureus*.

To validate the concentration of the bacteria, a spectrophotometer was used to measure the intensity value. As a control, the intensity of DI water was measured and recorded. In order to achieve serial dilution, 100 µl of the stock solution was added to 900 µl of LB. This step was used to achieve concentrations of 10^7 to 10^4 CFU/mL; stock solution was changed to the magnitude higher than the wanted concentration. 1mL of the bacteria sample was placed into a cuvette and the optical density at 600 nm was obtained from the spectrophotometer.

Smartphone Platform and Imaging Procedure

Fluorescence microscope for quantifying NK Cell subpopulation

To create the fluorescent particles, antibody specific to NK cell targets, including human polyclonal anti-IL-2 and recombinant human anti-CD56 were covalently conjugated to the carboxylated, green fluorescent, polystyrene nanoparticles with 500 nm diameter with a reported

488 nm excitation and 509 nm emission wavelengths. 1-ethyl-3-(3-dimethylaminopropyl) carbodiimide (EDAC) conjugation chemistry was used in the process of linking antibodies to nanoparticles [17].

The cell chromatography lane was imaged using a custom-built smartphone fluorescence microscope consisting of a smartphone (Samsung Galaxy S20), commercially available microscope attachment, 473 nm excitation LED light source, and an acrylic filter used as a 450 to 500 nm bandpass filter. A 3D printed housing was also created to hold all materials in one housing. In this case, a device was printed following the protocol described in Chung et al. (2021). The housing was created using SolidWorks, was converted to a gcode, loaded onto the 3D printer and printed from acrylonitrile-butadiene-styrene (ABS) polymer material with 1 μm resolution using black filament to create a dark environment. The LED light source serves to excite the fluorescent nanoparticles in the samples, and the acrylic filter is used as a low-cost light filter to selectively filter emitted light from the same nanoparticles. The LED emitted onto the paper chip from 15° angle. In a dark room, the smartphone captured 6 total field of views of the paper chip where the chip was moved manually under the microscope.

Set-up for Identification of Bacteria presence

Acrylic film was used as a low-cost optical bandpass filter, allowing only the wavelengths from 480 to 520 nm to pass through. The acrylic film was placed in front of the smartphone camera. A smartphone camera (Samsung Galaxy S20) was used to image bacterial droplets on surfaces. The droplets were placed on microscope slides or laboratory desks, and left to dry for 30 minutes. The “pro” mode of the smartphone camera was used in taking images which allowed for the manual control: white balance = 2300K, ISO = 200, shutter speed = 2 s. The smartphone was placed 10 cm above the droplets, perpendicularly. A 9-V battery was used to power the 405 nm

LED, which was held 20 cm away from the droplets to minimize light reflectance (Fig. 1). , six 20 μ L droplets of each bacteria dilutions were placed onto the clean desk surface and allowed to dry for approximately 1-1.5 hr, depending on when the droplets become fully dry. After the droplets were dry, images were taken by a smartphone with the acrylic film and the 405 nm LED irradiating from 0° angle.

Image analysis

Machine Learning for Cell Chromatography Lane

A python code was created to analyze smartphone images by quantifying the number of fluorescent particles. First, smartphone microscopic images were cropped to remove the excess background. Next, each image was first converted into an 8-bit grayscale image, then blurred using a Gaussian blur to allow for adaptive thresholding. Adaptive thresholding parameters (blocksize and C value) were selected using trial and error and then picking the parameters that resulted in the largest initial concentration and bright: dim ratio disparity in the data. The blocksize parameter represents the square size of the small matrix that scans across the image and takes the average of the intensities of each pixel within the box matrix to determine whether or not the central pixel should be thresholded to white or black. Meanwhile, the C value is an integer intensity value that is subtracted from the averaged blocksize intensity in order to offset any outside brightness effect. The thresholded images were then run through a particle detection algorithm which counted the number of white pixels within the thresholded image. In order to find the best machine learning model to use on the data points of fluorescent particles, a grid search was performed among support vector machine (SVM), k-nearest neighbor (kNN), and random forest (RF). The model with the best overall accuracy, RF, was then chosen as the best model for the system.

Autofluorescence Intensity Analysis

ImageJ was used to process and analyze the images taken by the smartphone. Images were first cropped to isolate the droplet and then were split into blue, green, and red channels. Since the expected autofluorescence was in the green wavelength range, only the green channel was used to analyze the images. Using the “measure” function, ImageJ generated the pixel intensities (ranging from 0 to 255; 8-bit) for all pixels, and provided the number of pixels (x_i) at specific pixel intensity (i), e.g., 20 pixels showing the intensity of 100, 30 pixels showing the intensity of 101, etc. The following equation calculates the average intensity, where the denominator represents the total number of pixels, and the numerator represents all pixel intensities summed up. As shown in the equation, pixel intensities < 10 were not counted because the signal would be from the background.

Overview of thesis

Gold-standard techniques that have been discussed mostly require a large/expensive equipment and have a long time-to-result. These reasons bring about the need for a rapid technique that requires minimal training to use. The aim of this research is to use smartphone cameras, which are extremely accessible, and the use of fluorescence phenomenon to create systems that decrease time-to-detect, are cheaper and less complex.

First is a smartphone-based paper microfluidic platform that is capable of quantifying NK cell subpopulation analysis and cell/cytokine quantification from buffy coat samples, all within an assay that takes less than 15 minutes to conduct. Subpopulations of NK cells include CD56dim and CD56bright; CD56dim NK cells can perform direct cytotoxic cell killing and CD56bright can produce cytokines and release stimulatory cues. It is believed that the ratio of NK cell subpopulations has a direct correlation to the overall patient immune functions. The gold standard

technique currently to find the subpopulation ratio is the use of a flow cytometry which requires an expensive device. This produces the need for a cheap and rapid method to detect and quantify subpopulations. The platform created utilizes a chromatography paper chip with a single flow lane unit that performs spatial separation of CD56^{dim} and CD56^{bright} cells suspended in buffy coat over its length using differential binding of anti-CD56 nanoparticles. A smartphone microscope combined with machine learning predictive modeling was used to analyze NK cell subpopulation differentiation. The cell subpopulation analysis using the smartphone platform was compared to a benchtop microscope and achieved 89% accuracy.

The second smartphone platform created is able to identify bacterial species in biological and clinical laboratory settings. Various bacterial species have been found to naturally exist on surfaces, including *Escherichia coli*, *Salmonella* Typhimurium, and *Staphylococcus aureus* that were investigated in this study. The current method to test laboratory surfaces for bacterial presence is by swabbing the surface and culturing the sample overnight. Other methods that exist require expensive equipment as well. The platform designed in the study is able to detect bacterial presence from laboratory surfaces using a smartphone and low-cost components without the need to culture or stain the sample. A 405 nm LED was used to excite the bacteria in order to produce an autofluorescence signal which was quantified to identify bacteria. A low-cost acrylic film could isolate the autofluorescence emission. ImageJ was used to process and analyze the images and quantify the emitted autofluorescence signal. This imaging platform successfully detected the presence of all three bacterial species from the heavily used laboratory surfaces. An exponentially decreasing trend was observed with decreasing bacterial concentration, and the limit of detection was 10^4 CFU/cm². It could also distinguish from tap water, protein (bovine serum albumin), and NaCl solutions from bacterial species.

Future directions

The work presented in this thesis is preliminary research towards a better understanding of the use of smartphone imaging and fluorescence in the field of biosensors. Both, the NK cell subpopulation detection, and the bacterial presence detection, can be continued and improved with further development and research to achieve more specific objectives.

For the NK cell subpopulation detection, the next steps may include the use of mice to better understand the subpopulation actions or creating a regression model to further improve the accuracy. For a mice model, the human NK cells may be injected into a healthy immunosuppressed mouse and extracted after some time and compare the subpopulations to NK cells that are extracted from a cancer-induced immunosuppressed mouse. The extracted blood can be performed over time (12 hours, 1 day, 5 days) to understand the subpopulation actions. Another direction this work can continue in is by acquisition of more datasets from the current method to create a regression model that can output more specific and meaningful ratios.

The bacteria presence project can further be investigated by the use of machine learning techniques. Each bacterial species has a unique autofluorescence spectrum which can be used to distinguish between the species. Using a similar method, analyzing the number of pixels at each bit value, and incorporating machine learning, the model can learn the specific spectrum to identify the species and based on the intensity of the signal, it can quantify and predict the concentration of bacteria.

Furthermore, the same methodology may be used for the detection of other biological targets such as fungi and viruses. Studies have shown that fungi fluoresce when excited at 300 to

350 nm light and emit at 410 to 430 nm [18]. The fluorescence is due to the proteins, specifically Tryptophan residues, which fluoresces at 330 nm [19]. Fungi also has NADH which can excite at higher wavelengths, but the intensity of the emission light is too low for the smartphone setup to detect.

Viruses contain nucleic acid genomes and a protein that surrounds it, capsid. Together, they form a structure called nucleocapsid which has shown autofluorescence in past studies [20]. Excitation wavelength varies depending on the type of virus but the general wavelength for its excitation is 270 nm [21]. The emitted wavelength has a low intensity at 410 nm. An improved image analysis is required to extract data from images but can be done by optimizing the setup.

References

- [1] S. Thakkar, D. Sharma, K. Kalia, and R. K. Tekade, “Tumor microenvironment targeted nanotherapeutics for cancer therapy and diagnosis: A review,” *Acta Biomaterialia*, vol. 101, pp. 43–68, Jan. 2020, doi: 10.1016/j.actbio.2019.09.009.
- [2] L. Ruggeri *et al.*, “Effectiveness of Donor Natural Killer Cell Alloreactivity in Mismatched Hematopoietic Transplants,” *Science (1979)*, vol. 295, no. 5562, pp. 2097–2100, Mar. 2002, doi: 10.1126/science.1068440.
- [3] S.-Y. Wu, T. Fu, Y.-Z. Jiang, and Z.-M. Shao, “Natural killer cells in cancer biology and therapy,” *Molecular Cancer*, vol. 19, no. 1, p. 120, Dec. 2020, doi: 10.1186/s12943-020-01238-x.
- [4] B. Ming *et al.*, “The Increased Ratio of Blood CD56^{bright} NK to CD56^{dim} NK Is a Distinguishing Feature of Primary Sjögren’s Syndrome,” *Journal of Immunology Research*, vol. 2020, pp. 1–7, Jul. 2020, doi: 10.1155/2020/7523914.
- [5] T. Michel *et al.*, “Human CD56^{bright} NK Cells: An Update,” *The Journal of Immunology*, vol. 196, no. 7, pp. 2923–2931, Apr. 2016, doi: 10.4049/jimmunol.1502570.
- [6] “Contamination in a Microbiological Laboratory,” *International Journal of Research Studies in Biosciences*, vol. 6, no. 4, 2018, doi: 10.20431/2349-0365.0604002.
- [7] M. Rennie, D. Dunham, L. Lindvere-Teene, R. Raizman, R. Hill, and R. Linden, “Understanding Real-Time Fluorescence Signals from Bacteria and Wound Tissues Observed with the MolecuLight i:XTM,” *Diagnostics*, vol. 9, no. 1, p. 22, Feb. 2019, doi: 10.3390/diagnostics9010022.

- [8] M. Shu *et al.*, “Porphyrin Metabolisms in Human Skin Commensal Propionibacterium acnes Bacteria: Potential Application to Monitor Human Radiation Risk,” *Current Medicinal Chemistry*, vol. 20, no. 4, pp. 562–568, Jan. 2013, doi: 10.2174/0929867311320040007.
- [9] J. Fyrestam, N. Bjurshammar, E. Paulsson, A. Johannsen, and C. Östman, “Determination of porphyrins in oral bacteria by liquid chromatography electrospray ionization tandem mass spectrometry,” *Analytical and Bioanalytical Chemistry*, vol. 407, no. 23, pp. 7013–7023, Sep. 2015, doi: 10.1007/s00216-015-8864-2.
- [10] R. M. Goulter, I. R. Gentle, and G. A. Dykes, “Issues in determining factors influencing bacterial attachment: a review using the attachment of *Escherichia coli* to abiotic surfaces as an example,” *Letters in Applied Microbiology*, vol. 49, no. 1, pp. 1–7, Jul. 2009, doi: 10.1111/j.1472-765X.2009.02591.x.
- [11] R. Kosif and F. Avcioglu, “An Examination of Bacterial Contamination of Models Used in Anatomy Laboratories,” *Interdisciplinary Perspectives on Infectious Diseases*, vol. 2018, pp. 1–5, Dec. 2018, doi: 10.1155/2018/9201312.
- [12] Y. T. Bryceson *et al.*, “Functional Analysis of Human NK Cells by Flow Cytometry,” 2010, pp. 335–352. doi: 10.1007/978-1-60761-362-6_23.
- [13] M. A. Cooper and M. A. Caligiuri, “Isolation and Characterization of Human Natural Killer Cell Subsets,” *Current Protocols in Immunology*, vol. 60, no. 1, Apr. 2004, doi: 10.1002/0471142735.im0734s60.

- [14] A. Cossarizza *et al.*, “Guidelines for the use of flow cytometry and cell sorting in immunological studies (second edition),” *European Journal of Immunology*, vol. 49, no. 10, pp. 1457–1973, Oct. 2019, doi: 10.1002/eji.201970107.
- [15] S. v. Angus, S. Cho, D. K. Harshman, J.-Y. Song, and J.-Y. Yoon, “A portable, shock-proof, surface-heated droplet PCR system for *Escherichia coli* detection,” *Biosensors and Bioelectronics*, vol. 74, pp. 360–368, Dec. 2015, doi: 10.1016/j.bios.2015.06.026.
- [16] K. E. McCracken, S. v. Angus, K. A. Reynolds, and J.-Y. Yoon, “Multimodal Imaging and Lighting Bias Correction for Improved μ PAD-based Water Quality Monitoring via Smartphones,” *Scientific Reports*, vol. 6, no. 1, p. 27529, Jun. 2016, doi: 10.1038/srep27529.
- [17] T.-H. Ulep *et al.*, “Smartphone based on-chip fluorescence imaging and capillary flow velocity measurement for detecting ROR1+ cancer cells from buffy coat blood samples on dual-layer paper microfluidic chip,” *Biosensors and Bioelectronics*, vol. 153, p. 112042, Apr. 2020, doi: 10.1016/j.bios.2020.112042.
- [18] E. V. Fedoseeva, S. V. Patsaeva, D. A. Khundzhua, E. V. Prudnikova, and V. A. Terekhova, "Excitation-dependent emission spectra of fungal fluorophores in terms of their similarity to fluorescence of dissolved organic matter," *Optical and Nanotechnologies for Biology and Medicine*, 118450J, May. 2021, [doi: 10.1117/12.2590882](https://doi.org/10.1117/12.2590882)
- [19] A. B. T. Ghisaidoobe, and S. J. Chung. “Intrinsic tryptophan fluorescence in the detection and analysis of proteins: a focus on Förster resonance energy transfer techniques.” *International journal of molecular sciences* vol. 15,12 22518-38. 5, Dec. 2014, doi: 10.3390/ijms151222518

- [20] Y. Sheng, and Y. Liu. “Nucleocapsid protein preferentially binds the stem-loop of duplex/quadruplex hybrid that unfolds the quadruplex structure” *Chemical Communications*, 57, 5298-5301. Apr. 2021, doi: 10.1039/D1CC01767E
- [21] A. Alimova, A. Katz, R. Podder, G. Minko, H. Wei, P. Gottlieb. “Virus Particles Monitored by Fluorescence Spectroscopy: A Potential Detection Assay for Macromolecular Assembly.” *Photochemistry and photobiology*. 80. 41-6. Apr. 2007, Doi: 10.1562/2004-02-11-RA-080.1.

APPENDIX A: NATURAL KILLER CELL DETECTION, QUANTIFICATION, AND
SUBPOPULATION IDENTIFICATION ON PAPER MICROFLUIDIC CELL
CHROMATOGRAPHY USING SMARTPHONE-BASED MACHINE LEARNING
CLASSIFICATION

Ryan Zenhausem^{1†}, Alexander S. Day^{1†}, Babak Safavinia¹, Seungmin Han², Paige E. Rudy¹,
Young-Wook Won², and Jeong-Yeol Yoon^{1,*}

¹Department of Biomedical Engineering, The University of Arizona, Tucson, Arizona 85721,
United States

²Department of Surgery, The University of Arizona College of Medicine, Tucson, Arizona
85721, United States

[†]These authors contributed equally to this work

*Corresponding author, E-mail: jyyoon@arizona.edu

Received: 4 June 2021; Received in revised form 1 December 2021; Accepted 22 December
2021

Published in Biosensors and Bioelectronics

Abstract

Natural killer (NK) cells are immune cells that defend against viral infections and cancer and are used in cancer immunotherapies. Subpopulations of NK cells include CD56^{dim} and CD56^{bright} which either produce cytokines or cytotoxically kill cells directly. The absolute number and proportion of these cells in peripheral blood are tied to proper immune function. Current methods of cytokine detection and proportion of NK cell subpopulations require fluorescent dyes and highly specialized equipment, e.g., flow cytometry, thus rapid cell quantification and subpopulation analysis are needed in the clinical setting. Here, a smartphonebased device and a two-component paper microfluidic chip were used towards identifying NK cell subpopulation and inflammatory markers. One unit measured flow velocity via smartphonecaptured video, determining cytokine (IL-2) and total NK cell concentrations in undiluted buffy coat blood samples. The other, single flow lane unit performs spatial separation of CD56^{dim} and CD56^{bright} and cells over its length using differential binding of anti-CD56 nanoparticles. A smartphone microscope combined with cloud-based machine learning predictive modeling (utilizing a random forest classification algorithm) analyzed both flow data and NK cell subpopulation differentiation. Limits of detection for cytokine and cell concentrations were 98 IU/mL and 68 cells/mL, respectively, and cell subpopulation analysis showed 89% accuracy.

Introduction

Natural killer (NK) cells are vital components of the innate immune system, capable of cytotoxic action and production of cytokines [1]. In peripheral blood, the actions of NK cells are broadly subdivided into two groups, based on their surface receptors: CD16-CD56⁻ NK cells (known as CD56^{dim} NK) and CD16-CD56⁺ NK cells (known as CD56^{bright} NK) [2]. These two subsets perform separate and complementary functions. CD56^{dim} NK cells perform direct cytotoxic cell killing via perforin and granzyme enzymes, whereas CD56^{bright} NK cells produce cytokines and release stimulatory cues [2]. Additionally, it is currently believed that CD56^{bright} NK cells are the immature precursors of the CD56^{dim} subpopulation [3]. The development of CD56^{bright} cells into CD56^{dim} cells is mediated by immune stimulatory cues, which also regulates the NK cell activity and cytotoxicity, namely cytokines such as interleukin 2 (IL-2), interleukin 12 (IL-12), and interleukin 15 (IL-15) [3,1].

In peripheral blood, the proportion of CD56^{bright} NK relative to CD56^{dim} NK is approximately 10%:90% , and these values, as well as absolute cell numbers, fluctuate slightly in healthy patients due to daily immune stimulation or suppression due to environment or exercise [4,5]. Chronic stimulation of the innate immune system drives NK cell exhaustion, apoptosis, and dysregulation, resulting in a dysregulation in the absolute cell numbers and the proportions between CD56^{dim} and CD56^{bright} subsets [6,7]. This can be particularly extreme in a variety of disease states ranging from viral infection to cancers. For example, several studies have shown that in head and neck cancers, the CD56^{dim} subpopulation is found to be significantly decreased [8]. These results are complemented by the studies in melanoma and autoimmune diseases, where changes in the relative proportion of CD56^{dim} NK cells have been found to inversely correlate with positive clinical outcomes [8,7]. As a result of the change in NK cell

subpopulations in disease states, CD56 expression in NK cells has been suggested as a diagnostic marker [9].

Given their innate and specific cytotoxic activity, NK cells have become an interesting target for cell-based immunotherapy [10]. Although chimeric antigen receptor T cells (CAR T cells) have dominated the cell-based therapy space previously, these therapies have significant side effects including cytokine release syndrome, neurological toxicity, and occurrence of graft versus host disease (GvHD), when T cells are derived from allogeneic sources [11]. The advantage of NK cells is that they have a better safety profile via their recognition of major histocompatibility complex (MHC) class 1 molecule down-regulation in diseased states, and reduced onset and severity of GvHD in patients [12,13]. When administering these NK cell-based therapies, the immune microenvironment status of the patient (including the cytokine stimulatory molecules) must be measured to appropriately dose the cell-based drugs being delivered to the patient. Additionally, as discussed above, tracking the absolute number and relative amount of NK cell subpopulations is a robust method to monitor disease progression and patient prognosis. Currently, the quantification of these biological signals is done using flow cytometry [14,15]. This method is the gold standard for immune cell subpopulation quantification. However, it is limited in the patient-facing application of NK cell-based therapy given the use of multiple fluorophores, expensive and large equipment, and the need for highly trained personnel. Microfluidic approaches have been demonstrated in recent years as portable, low sample volume, and accessible point-of-care alternatives to flow cytometry [16]. A large variety of microfluidic chips exist for the quantification of a wide variety of biological targets, including immune cells [17].

Although traditional microfluidic approaches are more apt for point-of care diagnostics, many devices rely on complex chip fabrication techniques that limit their wide implementation. Paper-based microfluidic platforms can overcome this challenge given their ease of fabrication, inherent pump-free mechanism via capillary action, and easy integration with widely available imaging platforms, including smartphone imaging systems [18,19]. However, given the 3D fibrous structure and optically opaque properties of paper, use of fluorescent dyes has been traditionally difficult on paper substrates given the presence of autofluorescence and backscattering of paper fibers [20]. Previous paper-based devices have shown the ability of flowbased detection methods to quantify cell number in a point of care fashion [21]. Additionally, previous paper-based microfluidic devices have utilized fluorescent nanoparticles, which benefit from superior stability and sensitivity compared to traditional fluorescent dyes, to enable on-chip smartphone-based imaging [22]. Although these microfluidic platforms can perform highly accurate quantification of biological targets for diagnostics, no papers to our knowledge have shown the application of microfluidics for NK cell-based therapy prognostics. In the case of NK cell-based therapy, there exists a need to quantify the patient's innate immune status to determine the potency and dosing of treatment.

In this work, we have developed a paper microfluidic device with two quantification zones: the first for both cytokine and cell number analysis via flow velocity measurements and the second for NK cell subpopulation analysis using direct on-chip smartphone-based imaging coupled with automated image analysis and machine learning classification. Figure 1 shows the schematic illustration of this work.

Although cell chromatography has been demonstrated before, including for isolation of lymphocytes directly from whole blood as per Mohr et al., 2018, this process is limited in that it

is unable to distinguish subpopulations of the same cell type [23]. Additionally, although paperbased approaches are point-of-care and simple, direct on-paper imaging is typically noisy and difficult to perform. The addition of antibody conjugated, fluorescent nanoparticles, allows us to amplify optical signals from cell separations. Where direct imaging of cell subpopulations is not perfect, application of machine learning methods allows for the generation of high dimensional, complex data which can be effectively classified to a high degree of accuracy. To the best of our knowledge, no work has been demonstrated for the paper microfluidic- and smartphone-based cell subpopulation analysis that can substitute and rival the benchtop flow cytometry equipment. In addition, the use of machine learning predictive modeling (in this case random forest classification) for analyzing paper microfluidic cell chromatography has not been demonstrated.

Overall, the assay developed provides a rapid, easy to manufacture, point-of-care method to quantify both IL-2 cytokine and NK cell concentrations, as well as NK cell subpopulations, using flow and imaging-based methodologies coupled with an advanced image processing and machine learning pipeline. This novel device offers key cost and implementation advantages over current technologies, enabling prognostics for autologous NK cell-based therapy. This work can be applied to wide-ranging applications since it can be used to many other cytokines and cell subpopulations for disease diagnostics and prognostics.

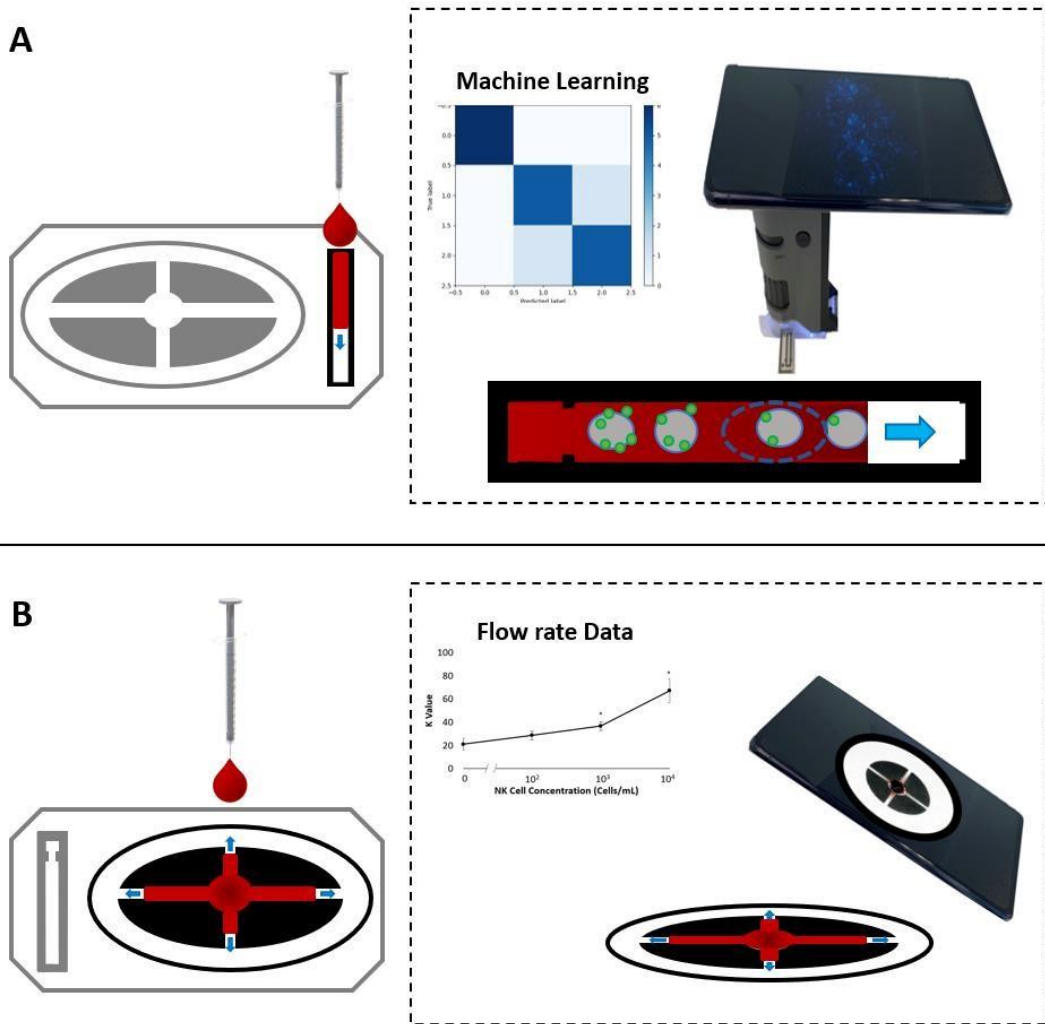


Figure A-1. Paper microfluidic chip layout and assay procedure. Buffy coat blood sample is pipette-added to the single-channel cell chromatography lane in the right (A) and the fourchannel flow lane in a circular layout in the left (B). A smartphone fluorescence microscope captures the fluorescence microscopic images from a cell chromatography lane (A). Anti-CD56 conjugated fluorescence nanoparticles are used and binding of anti-CD56 particles slows down the movement of NK cells through paper pores (A). Anti-IL-2 and anti-CD56 conjugated nanoparticles are used and a smartphone captures the video of such flow and the flow profile is obtained (B). Cell chromatography images and flow data are fed into analysis codes and outputs results for machine learning classification (A) and flow rate (B).

Materials and Methods

Cell Culture and Confirmation of Surface Expression

Contact independent natural killer cells (NK-92; ATCC, Manassas, VA, USA) were cultured in TheraPeak X-Vivo-15 media (Lonza; Walkersville, MD, USA) supplemented with 10% v/v fetal bovine serum (FBS; 30-2021; ATCC; Manassas, VA, USA) and 250 units/mL (0.2 ng/mL) of interleukin-2 (IL-2; 78036; StemCell, Cambridge, MA, USA) to stimulate cell proliferation. Interleukin-6 (IL-6; 200-06; PeproTech, Princeton, NJ, USA) was used for crossreactivity of the flow platform against IL-2. Cells were cultured at 37°C and 5% CO₂ in an incubator (HERA cell 150i; Cambridge Scientific; Watertown, MA, USA) and media was changed based on one of two subculture techniques to produce NK-92 cells with both high and low expression of CD56. Standard cell subculture was performed for the NK-92 CD56^{bright} subpopulation in which cell concentration was determined via a hemocytometer, cells were pelleted by centrifugation at 1,500 RPM for 5 min and resuspended in fresh media at 500,000 cells/mL every three days. To produce the NK-92 CD56^{dim} subpopulation, cells were maintained in an IL-2 poor media by extending the subculture time to >1 week. Cell concentration was determined via a hemocytometer and additional media was added to the flask to maintain cells at a concentration of 500,000 cells/mL.

After two weeks of cell subculturing, cell surface expression of CD56 was quantified via flow cytometry (LSR II; BD, Franklin Lakes, NJ, USA). CD56^{dim} and CD56^{bright} NK cells were harvested, pelleted, and washed using Dulbecco's phosphate buffered saline (DPBS; 14190136; ThermoFisher Scientific, Waltham, MA, USA). Both cells were incubated with APC-conjugated anti-CD56 antibody (130-113-305; Miltenyi Biotec, Bergisch Gladbach, Germany) according to manufacturer's instruction. In subsequent, the cells were triplicate washed using DPBS and

centrifuge to remove free APC-conjugated anti-CD56 antibody. The cells were then suspended in DPBS for further flow cytometry analysis. Flow cytometry analysis was conducted to verify that we had distinguishable CD56 expression on NK cells.

Particle Conjugation and Specificity Analysis

Antibodies specific to cytokine and NK cell targets, including human polyclonal anti-IL-2 (500-M02; Peprotech, Rocky Hill, NJ, USA) and recombinant human anti-CD56 (130-108016; Miltenyi Biotec, Bergisch Gladbach, Germany) were covalently conjugated to the carboxylated, green fluorescent, polystyrene nanoparticles with 500 nm diameter (CAYF500NM; Magsphere Inc., Pasadena, CA, USA) with a reported 488 nm excitation and 509 nm emission wavelengths. 1-ethyl-3-(3-dimethylaminopropyl)carbodiimide (EDAC) conjugation chemistry was used in the process of linking antibodies to nanoparticles as described by Ulep et al., which has been well documented for several decades [21,24]. Three batches of anti-IL-2 and five batches of anti-CD56 polystyrene nanoparticles were used throughout experiments to reduce batch-to-batch variability in results.

Particles were added to their respective targets (IL-2 and NK cells with varying CD56 expression) to assess the specificity of the antibody conjugated nanoparticles. For anti-IL-2 specificity, 50 μ L of antibody conjugated nanoparticles with a stock antibody concentration of 1 mg/mL and IL-2 samples diluted in DI water (for the sake of dilution; buffers are used for the other solutions and thus present in the final suspension) were combined, and five brightfield images were taken from a benchtop microscope (Eclipse TS100; Nikon Corp.; Tokyo, Japan) at 100X for each concentration after 5 min of incubation at room temperature. ImageJ (U.S. National Institutes of Health, Bethesda, MD, USA) was used to determine the number of particle aggregates for each concentration. In this, images were thresholded, binarized, and constructs

greater than 190 pixels were counted as particle aggregates using the “analyze particles” function. To assess anti-CD56 particle specificity, 50 μL of particles were added to 50 μL of NK-92 cells (both CD56^{dim} and CD56^{bright}) diluted to 10^5 cells/mL. After a 5 min incubation period, 10 μL of the mixtures were added to a glass slide with coverslip to prevent evaporation and brightfield and fluorescent images were acquired with a benchtop microscope at 100X. Brightfield and fluorescent images were stacked using ImageJ where the number of cells in each image, as well as the number of particles attached to each cell, were counted for all images manually.

Paper Microfluidic Chip Design, Fabrication, and Assay Procedure

The paper microfluidic chip is composed of two major chambers, the flow lanes used to quantify cell and cytokine concentration, and the cell chromatography lane, used to quantify NK cell subpopulations, as shown in Figure 1. SolidWorks (Dassault Systemes, Velizy-Villacoublay, France) was used to design the wax-printed channels. Four 5 mm x 2 mm channels are aligned in a circular manner sharing the central inlet to allow for capillary flow measures. There is a separate 8 mm x 2 mm channel for cell chromatography. The complete paper chip is composed of grade 1 chromatography paper (Whatman Grade 1 Chr; GE Healthcare, Maidstone, Kent, UK), chosen particularly for its 20 μm pore size relative to the NK cell size (6-10 μm), with wax barriers printed using a wax printer (ColorQube 8580; Xerox, Norwalk, CT, USA) that provide an intact hydrophobic barrier throughout the depth of the paper after melting on a hotplate at 120°C for 2 min.

Once paper chips were designed and prepared, samples of both IL-2 and NK-92 cells (containing physiologically relevant amounts of CD56 expression) were diluted in 1X buffy coat (SER-BC-SDS; ZenBio, Research Triangle, NC, USA). Samples were created for both cell and cytokine quantification as well as cell subpopulation analysis. For the flow lane samples, IL-2

samples were serially diluted from 250 IU to 75 IU and NK cell samples were diluted from 10^6 cells/mL to 10^3 cells/mL. NK cell mixtures were additionally prepared by sonication for 5 min in 1-min increments to mechanically lyse the cells and release the bulk of surface antigens, including CD56, into solution. 80 μ L of spiked IL-2 or NK cell buffy coat samples were mixed with 40 μ L of their respective antibody conjugated nanoparticles and allowed to incubate for 5 min at room temperature. For the cell subpopulation samples, intact NK cell subpopulations were mixed in ratios ranging from 100%:0% to 60%:40% CD56^{dim} and CD56^{bright} NK cells, at a concentration of 10^5 cells/mL, and antibody conjugated nanoparticles were added and allowed to incubate for 5 min at room temperature. Since this NK cell concentration is substantially higher than those in the normal buffy coat samples (10^6 cells per 100 mL sample) but comparable to that after NK cell therapy and the emphasis is the determination of the bright:dim cell ratio, our bright:dim ratio assay is largely determined by our mixtures and not by the innate NK cells present in the sample [25].

To perform the assay, 5 μ L of cell subpopulation sample was added to the cell chromatography lane and allowed to flow and dry for 5 min. Meanwhile, 5 μ L of 0.05% (v/v) Tween-20 was added to the center of the flow chamber and allowed to dry for 3 min. 15 μ L of flow lane samples (containing cytokines or lysed cells) were added to the flow lane chamber of the microfluidic chip and videos were taken via smartphone (Galaxy S20; Samsung, Suwon, South Korea) at 30 FPS (frames per second) over the course of the flow duration. The cell chromatography lane was then fluorescently imaged at 100X by taking 6 sequential fields of view for the benchtop microscope and 5 sequential fields of view for the smartphone microscope along the chip length from inlet to outlet (differences in image count are due to the relative scale of the images being different between the two imaging modalities). Experiments were performed

over multiple days to account for batch-to-batch variation in samples, to allow for natural fluctuations in CD56 expression as would be seen in clinical samples.

Design and Optimization of Smartphone Fluorescence Microscope

The cell chromatography lane was imaged using a custom-built smartphone fluorescence microscope consisting of a smartphone, commercially available microscope attachment (MP-250 MicroFlip 100x-250x Pocket Microscope; Carson Optical, Ronkonkoma, NY, USA), 473 nm excitation LED light source (XPEBBL-L1-0000-00302; Cree Inc., Research Triangle Park, NC, USA), and an acrylic filter used as a 500 nm bandpass filter (510 AY 25; Comar Optics, Cambridge, UK). A 3D printed housing was also created to hold all materials in one housing. In this case, a device was printed following the protocol described in Chung et al., 2021. In short, the design, created using SolidWorks, was converted to a .gcode file type, loaded onto the 3D printer (Crealty Ender 3; Creality, Shenzhen, China) and printed from acrylonitrile-butadienestyrene (ABS) polymer material with 1 μm resolution using black filament to create a dark environment. The LED light source serves to excite the fluorescent nanoparticles in the samples, and the acrylic filter is used as a low-cost light filter to selectively filter emitted light from the same nanoparticles. The device had multiple holes to be assembled using simple 3 mm screws.

Given the inherent noise in images created by reflection from the paper fibers, optimal imaging conditions were determined by varying light source angle and drying time. This was performed to optimize the signal-to-noise ratio between no target samples and samples containing target. To do this, samples containing either buffy coat or CD56^{bright} NK cells and particles in buffy coat were added to a cell chromatography lane and allowed to dry for various time points. Additionally, the incident angle of the LED light source was varied in three

conditions: 45° above, 0° below, and 15° below the paper chip. Three images were captured using the smartphone fluorescence microscope device described above with fixed imaging parameters (2-second integration time, 400 K white balance, and -2.0 auto focus). Images were then analyzed using ImageJ to quantify average intensity. Similar to benchtop experiments, trials were conducted over multiple days to account for batch-to-batch variability in samples.

Microscopic Image Analysis and Machine Learning Model for Cell Chromatography Lane

For each microscopic image of the fluorescent particles, Python code was used to extract the relevant data. This included the use of the Pillow and OpenCV libraries for image analysis and adjustment, as well as SciPy for automated particle detection using the `scipy.ndimage.measurements.label()` function. For the smartphone microscopic images, the image was first cropped to get rid of excess black areas around the central microscopic image, but otherwise the image analysis algorithm was identical. Each microscope image was first converted into an 8-bit grayscale image, then blurred using a Gaussian blur to allow for subsequent adaptive thresholding. Adaptive thresholding parameters (blocksize and C value) were selected using a grid search and then selecting the parameters that resulted in the largest initial concentration and bright:dim ratio disparity in the data. The blocksize parameter represents the square size of the small matrix that scans across the image and takes the average of the intensities of each pixel within the box matrix to determine whether or not the central pixel should be thresholded to white or black. Meanwhile, the C value is an integer intensity value that is subtracted from the averaged blocksize intensity in order to offset any outside brightness effect (such as an external light source). The thresholded images were then run through two separate particle detection algorithms: one from the SciPy library that automatically detected individual features within the image that it determined to be separate, and one that was developed

independently by the authors that counted the number of white pixels within the thresholded image. An additional algorithm was developed that could check for particle aggregation by comparing the distances between each particle within the image and determining if they were aggregated based on predefined distance parameters, but this increased the time of analysis immensely on the smartphone microscope platform, and thus was not included in the smartphone system.

Each microscopic image therefore had 4 or 2 data points designated to it (depending on whether images were taken via benchtop or smartphone microscope, respectively): the number of particles counted by the automatic SciPy algorithm, and the number of white pixels counted by the self-made algorithm. Each lane would have several microscopic images attached to it, each of which had two data points assigned to it after analysis. As extracted parameters within each individual image would have large error bars associated, making it nearly impossible to determine significance within a single image, all images taken for one chip are combined into one observation of size one by twenty-four for the benchtop microscope images (as there are four data points for six total images per single chip) and one by ten for the smartphone microscope images (as there are two data points for five total images per single chip). These series of double data points were then saved for each lane to a .csv file, along with the relative bright:dim ratio for each lane. This .csv file was then used as the dataset for supervised machine learning model development, with one model being developed for the benchtop microscope platform, and one for the smartphone microscope platform. The machine learning models were developed using Python and the Scikit-Learn library, a popular machine learning library allowing for the development of many different algorithm types. The final model was developed by using a grid search that determined 1) the best model type among support vector machine (SVM), k-nearest

neighbor (kNN), and random forest (RF), 2) best model hyperparameters that varied depending on the model type, and 3) best data scaling option among no scaling, MinMax scaling, and StandardScaling, all of which can be found in the Scikit-Learn documentation, in conjunction with 4) leave-one-out cross validation, which was utilized due to the relatively small number of data points. The models with the best overall accuracy were then chosen as the best models for the system.

The overall pipeline from cell chromatography image acquisition to insertion to the machine learning database can be seen in Figure 2. The database illustrated is then used for machine learning model development.

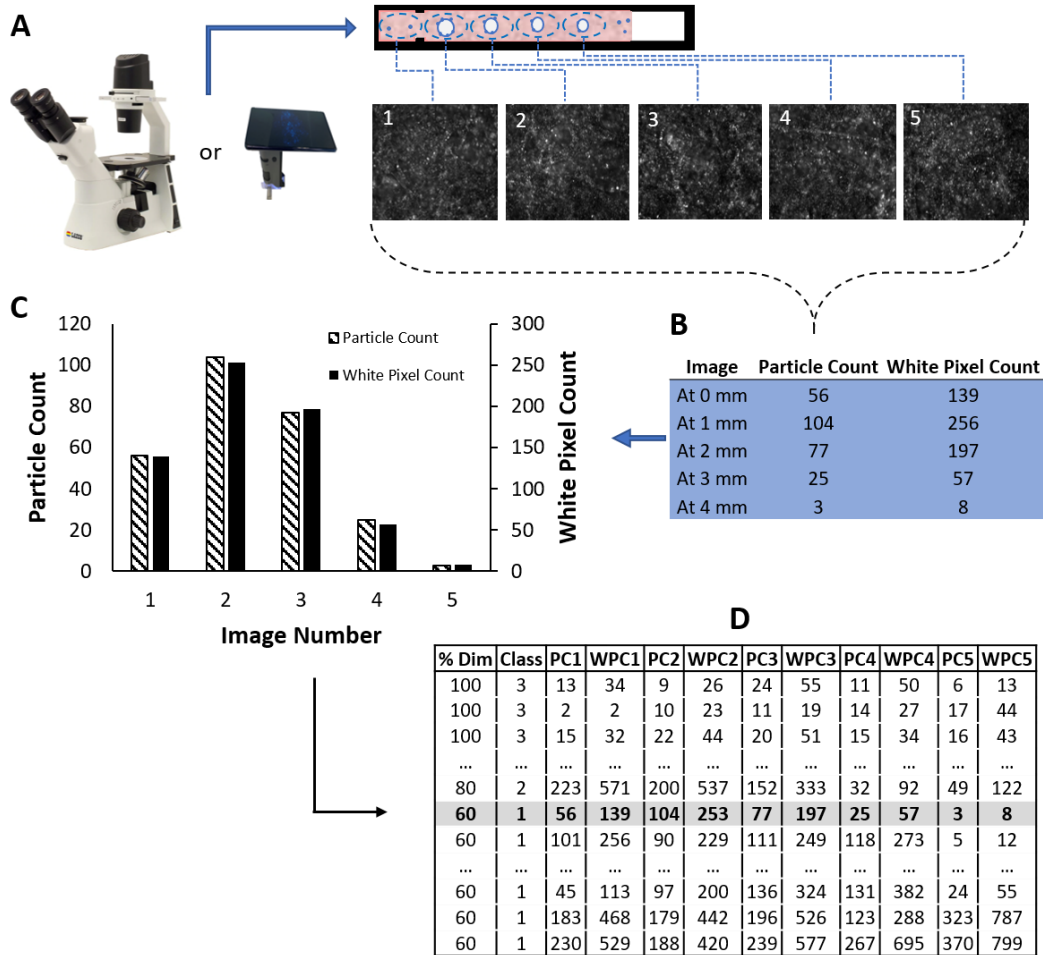


Figure A-2. Image analysis/database generation pipeline. A) multiple benchtop or smartphone microscope images are taken sequentially starting from the sample input and moving outward at regular intervals. B) Microscope images are analyzed to extract out relevant data from each image, thus associating each image with multiple data points. C) The extracted data represents a cell chromatography profile, which is generated for each chip and has multiple dimensions of data. D) This data is saved to a database, along with the known CD56^{dim} ratio, to allow for machine learning model generation after the database has been completed.

Video Analysis and Data Extraction for the Flow Lane

Video was captured to collect the flow profile before the sample was dropped onto the paper microfluidic chip center. This ensured that the beginning moments were always captured, as these moments were key to obtaining relevant data (video frames prior to sample inclusion were then cut from the final video prior to analysis). Videos were always captured in the same light setting and always at the same distance from the paper chip to ensure that there was no variation in lane length in pixels. Videos were captured for 30 seconds after the sample was dropped onto the paper chip, where the videos were then saved to be analyzed.

Video analysis was conducted using Python, including the OpenCV for image analysis and adjustment and SciPy for fitting to a proposed flow model. To measure flow distance, the analysis algorithm first converted the image to grayscale and then was told by the user where the initial flow profile began (the entrance to the four flow lanes) to get rid of any variation in paper chip placement relative to the smartphone camera. The algorithm then created an array that looked through the 180 pixels outward from the center of the paper chip every frame to see if there was a significant change (>18 brightness intensity drop) in any pixels, where the total number of pixels that had such a significant drop was then summed up. This sum represents the length of the sample flow in pixels, as the flow of the sample causes a darkening of the paper chip as it moves, which is then measured by the algorithm. The number of darkened pixels per frame is then saved to an array, which becomes the flow profile of the lane (with each array index representing a single frame within the video). This flow profile was then originally fitted to a Lucas-Washburn equation using SciPy, with the reasoning being that the flow velocity is fast as the sample is first introduced, before slowing. The Lucas-Washburn equation is described as (Klug et al., 2018):

$$\frac{d^2}{t} = \frac{R\gamma_{LG}\cos\theta}{2\mu}$$

where d is the flow distance, t is time, R is the pore size (originally the capillary radius), γ_{LG} is the interfacial tension at the liquid-gas interface, θ is the water contact angle at the paper pore (originally the capillary wall), and μ is the viscosity of the solution. Assuming that R and μ do not change much upon particle aggregation (as confirmed by Klug et al., 2018), the particle aggregation would primarily change the interfacial parameters γ_{LG} and θ . These interfacial effects can be lumped together into K :

$$d = K\sqrt{t}$$

However, this model does not adequately describe the flow profiles seen in the videos, as the flow does not continue infinitely (which would normally happen with a square-root relationship), and the particle aggregation continued to occur as the liquid flowed through the paper pores. Because of this dynamic process, the flow profile is in fact fast at first and then slows, the flow profile plateaus to a set point that was the same for all samples regardless of target concentration. Therefore, it is important to extract the initial slope from this flow profile, where MichaelisMenten-like equation can adequately be used:

$$d = d_{max} \frac{t}{K + t}$$

where d is the flow distance, t is time, d_{max} is the maximum distance reached by sample (set to the same value for all samples), and K is the value that determines the initial flow speed (fitted using SciPy code). When the analysis came up with a final K value that best fit the data, the K values was then compared across initial antigen concentrations to determine if there was a relationship.

Results and Discussion

Confirmation of Differential Particle Binding to IL-2 and NK-92 Cells

Antibody conjugated nanoparticles specific for both cytokine IL-2 (via anti-IL-2) and NK-92 cells (via anti-CD56) were tested for their target binding capability to characterize their functionality. Figure 3A shows the number of aggregated anti-IL-2 particles for the IL-2 target diluted in DI water for a range of target concentrations. The extent of antibody-antigen binding induced aggregation linearly increased and leveled off, with all concentrations showing statistically different extent of aggregation from the zero concentration ($p < 0.05$). To additionally test anti-CD56 particle's binding and subsequent aggregation, NK-92 cells separated into respective subpopulations via fluorescence-activated cell sorting (FACS) were combined with anti-CD56 nanoparticles and imaged on a glass slide under a benchtop microscope. Once brightfield and fluorescence images are overlaid, a frequency histogram was created to assess the number of particles bound to cells. As seen in Figure 3B, CD56^{bright} cells show a higher frequency of cells with >2 particles/cell compared to CD56^{dim} cells that have a peak at 1 particle/cell. CD56^{bright} cells also show a larger range of particle binding (from 1-9 particles/cell) compared to CD56^{dim} cells (0-5 particles/cell). The right shift in the frequency histogram for CD56^{bright} cells compared to CD56^{dim} cells shows a differential binding pattern between cell subpopulations, which is expected given the difference in CD56 surface expression between subpopulations. However, significant overlap exists between CD56^{dim} and CD56^{bright} cells in this histogram, indicating that conventional analysis would not work to make a clear distinction between these two subpopulations.

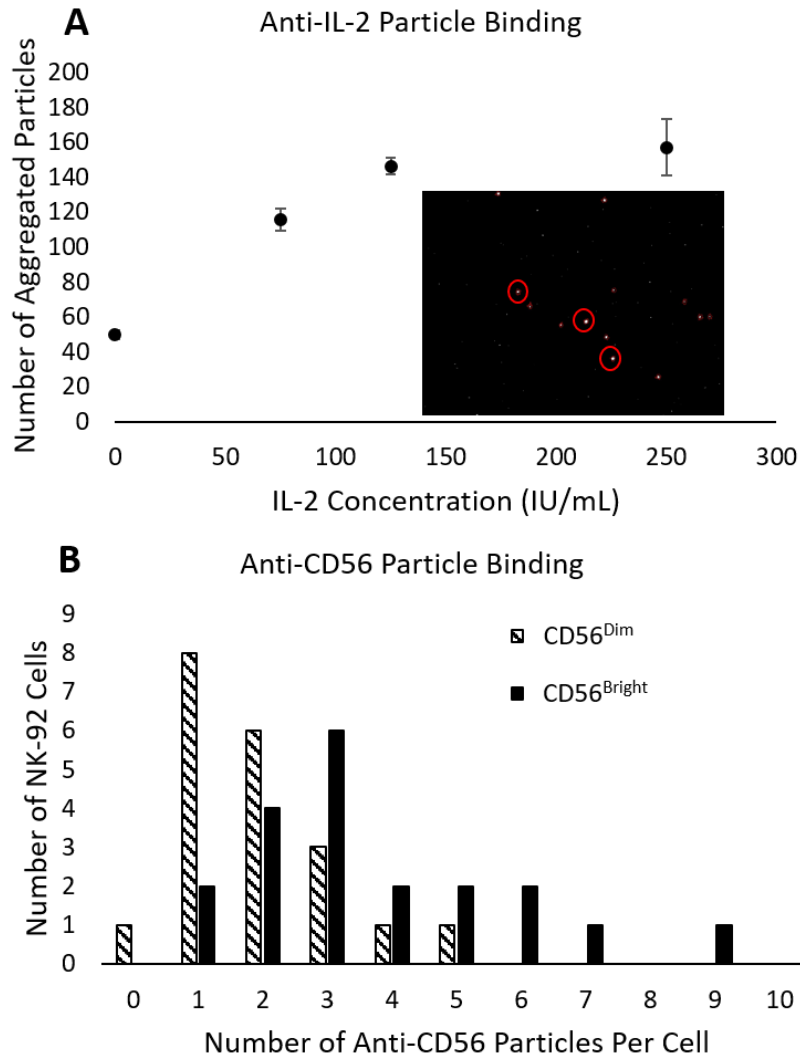


Figure A-3. Confirmation of antibody conjugated particles' binding to IL-2 and NK-92 cells. A) Anti-IL-2 conjugated particles show the increased number of particle aggregates with increased IL-2 concentration and a representative microscope image where the red circles indicate locations where particles were found to have aggregated. Error bars represent standard error with $n = 3$. B) Anti-CD56 conjugated particles bind to two different subpopulations (CD56^{dim} and CD56^{bright}) of NK-92 cells, with different binding extents to each subpopulation.

Flow Profile Measurements from Smartphone Videos

The relative concentrations of IL-2 and NK cells within spiked buffy coat blood samples was determined using flow profile analysis. To determine if there was a relationship between the amount of IL-2 within a sample and the sample's corresponding flow profile, various amounts of IL-2 were added to buffy coat samples, and the flow rate profiles – plots of distance (d) against time (t) – were obtained. Michaelis-Menten-like equation was used to evaluate the initial slope d_{max} / K (see section 2.6), and the extracted K values from these sample's flow profiles (with $n = 3$) were plotted against IL-2 concentration. Similarly, to determine if there was a similar relationship between NK cell concentration and flow profile, the extracted K values from the corresponding flow videos were also analyzed. In Figures 4A and 4B, there is a general increase in the extracted K value as the initial IL-2 units increases, and in Figures 4C and 4D, there is also an increase in the K value as the NK-92 cell concentration increases. Using regression analysis, the limit of detection of these flow assays is 98 IU/mL IL-2 and 68 NK cells/mL. When converting to ng/mL for the cytokines (1 IU IL-2 = 0.1 ng IL-2), the limit of detection of both the cytokine and cell assay are comparable to existing platforms [21,26]. Park et al. reported the LOD of 2.6 million NK cells/mL for the flow cytometric measurement and impedance-based assay, and Zhu et al. reported the LOD of 25,000 cells/mL using electronic cell sensor arrays [27,28]. IL-6 was used as a cross reactive cytokine to evaluate assay specificity, and the results for these flow profiles, seen in Figure 4B, show no significant increase when compared to the target of interest.

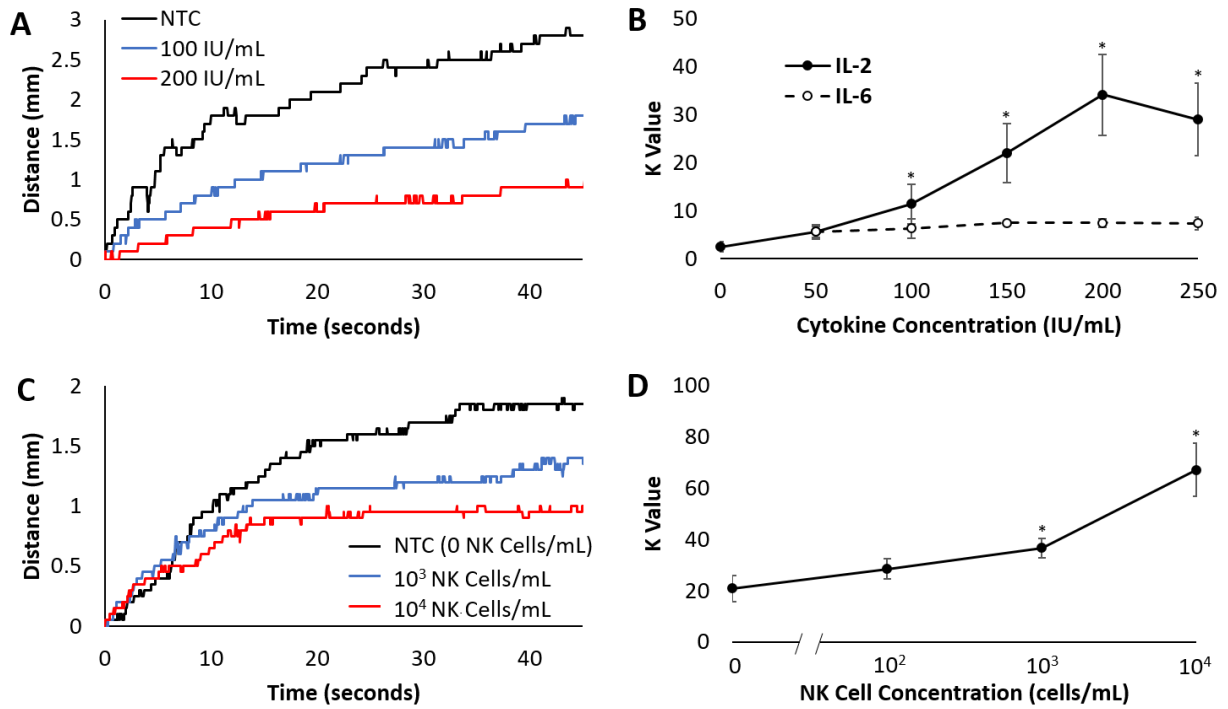


Figure A-4. Flow profile measurements. A) Representative d (flow distance, mm) vs. t (time, s) plots for assaying IL-2. All raw plots are available in Supplementary Figure S1. B) Average K vs. IL-2 (target cytokine; solid line) and IL-6 (for cross-reactive experiments; dashed line) concentration (IU/mL) plot ($n = 3$). Error bars represent standard errors. * represents a significant difference from non-cytokine-spiked buffy coat samples ($p < 0.05$). Dashed line represents K values C) Representative d vs. t plots for assaying NK-92 cells. All raw plots are available in Supplementary Figure S2. D) Average K vs. NK-92 cell concentration (cells/mL) plot ($n = 3$). Error bars represent standard errors. * represents significant difference from non-cytokine-spiked buffy coat samples ($p < 0.05$).

Cell Separation Validation on Chromatography Lane

To validate the efficient and measurable separation of NK-92 cell subpopulations over the length of the cell chromatography lane of the paper microfluidic chip, known ratios of CD56^{dim} and CD56^{bright} NK-92 cells were diluted to 10^5 cells/mL in buffy coat, and added alongside the fluorescent nanoparticles (conjugated with anti-CD56) to the chromatography lane, and subsequent fluorescence microscope images were taken sequentially from inlet to outlet (in the manner seen in Figure 5A). After fluorescence images are acquired, brightness and contrast of images were adjusted and cells were counted. When analyzing the fluorescent particle count and white pixel count from these images across the chromatography lane, a chromatography profile can be seen for each channel. When comparing these profiles between different CD56^{dim}:CD56^{bright} ratios, the particle count and white pixel count peaks move out from the sample insertion point when there are a larger proportion of dim cells when compared to bright cells. Figures 5B and 5C show sample chromatography profiles which illustrate this point, as the 100% dim cells flowed farther into the chromatography lane than the 60% dim and 40% bright cells, i.e., a significant right shift in the location of CD56^{dim} compared to CD56^{bright} NK cells.

This right shift in the location of CD56^{dim} cells compared to CD56^{bright} cells is likely due to the factors including inherent size differences between the subpopulations (IL-2 starved CD56^{dim} NK-92 cells are smaller than the CD56^{bright} NK-92 cells), as well as the effects of differential anti-CD56 particle binding on the cell flowing through the paper pores by capillary action. In this case, higher CD56 expression results in more particle binding and increased flow resistance.

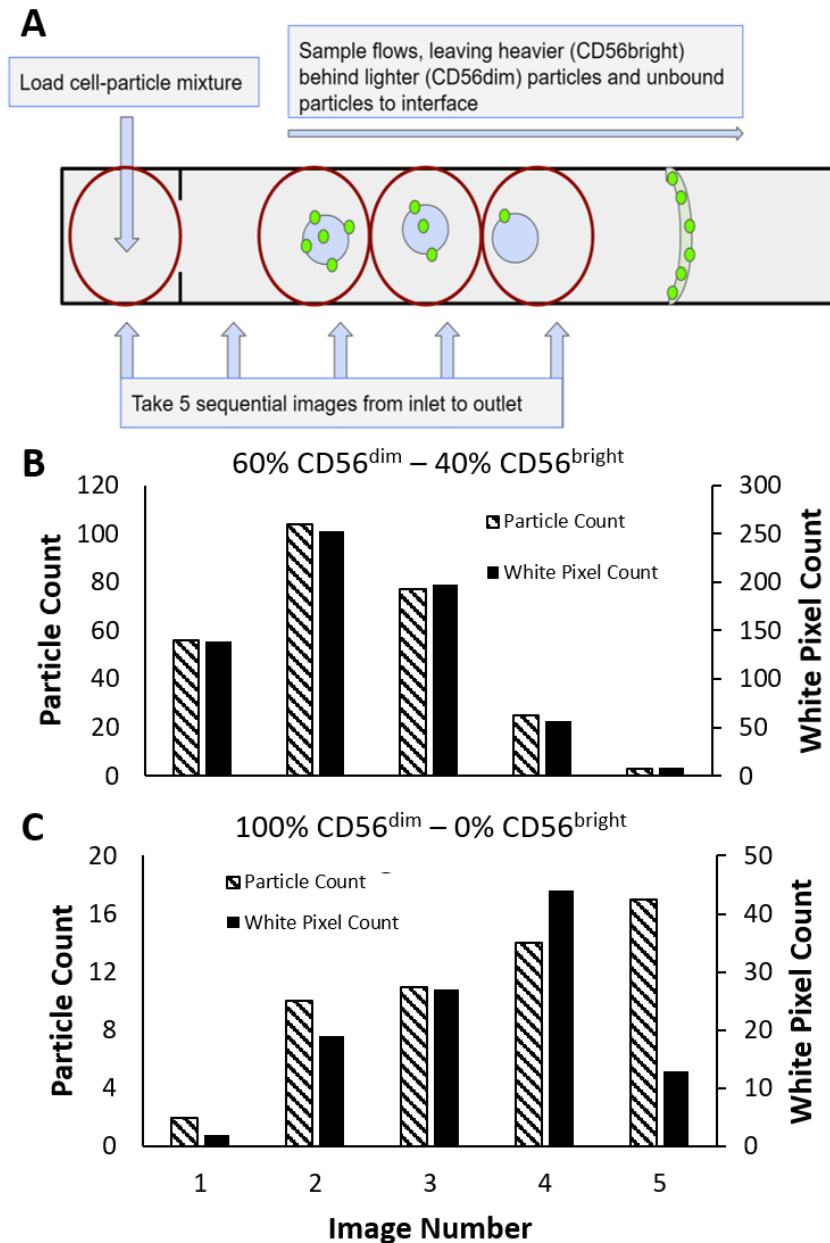


Figure A-5. Cell chromatography principle. The schematic diagram (A) of the cell chromatography lane of the microfluidic chip in which cell subpopulations are separated along the chip length via capillary flow, augmented by the effect of particle binding. Example cell chromatography profiles for samples containing CD56^{dim}:CD56^{bright} ratios of 60:40 (B) and

100:0 (C) can be seen, representing how samples with a larger proportion of CD56^{dim} cells tend to have higher fluorescent profiles further down the chip due to the principle seen in (A).

Cell Chromatography with Benchtop Microscope

Using benchtop microscope images obtained from 18 different chips (6 chips for each of the 3 bright:dim ratios; Figure 2A), the microscope images were then fed into the image analysis (which resulted in the construction of a database whose head can be seen in Figure 2B) and machine learning algorithms, where the overall model performance was then determined. The image analysis algorithm first thresholded the images using an adaptive thresholding technique whose parameters were optimized using grid-search, then used both a SciPy automated particle detection method and an independently-created algorithm, which detected the total number of white pixels within the image (the first two data points utilized). These two data points were finally used an independently-created algorithm to count the number of pixels that were sufficiently close to nearby pixels to indicate that they were bound to a cell together and also calculate the proportion of pixels that fit this “bound” category (the final two data points). This resulted in each image having four data points, thus causing the dataset used for machine learning model development to have 18 observations with 24 features each (4 for all 6 images) (Figures 2C and 2D). The machine learning model was developed using Leave-One-Out cross validation due to the relatively low amount of data points available. The processed data used for the training model are summarized in Supplementary Table S1. Using these algorithms, the final model was random forest-based, and had an accuracy of 89%.

Cell Chromatography with Smartphone-Based Fluorescence Microscopy

Cell chromatography experiments and subsequent machine learning analysis were repeated using a smartphone-based fluorescence microscope. Figures 6A and 6B show the schematic illustration and the photograph of the smartphone-based fluorescence microscope. When imaging the cell chromatography lane of the microfluidic chip, significant noise from the paper fibers becomes apparent when the chip is wet with buffy coat samples. To identify the LED angle and drying time that optimizes the signal-to-noise ratio (SNR), images were acquired using the smartphone-based fluorescence microscope for 1) buffy coat only samples and 2) the cells and particles in buffy coat samples. Average intensity values are extracted from the images using ImageJ. Figure 6C shows the results for the LED placed at a 15° incident angle below the paper microfluidic chip. Significance of $p < 0.01$ is achieved for the 5-min drying time, where other angles and drying times do not rival this level of significance. Data with the other angles are available in Supplementary Figure S3. With this set up, we maximized the significant SNR such that paper reflection of light is minimized and capture of fluorescence of nanoparticles is maximized.

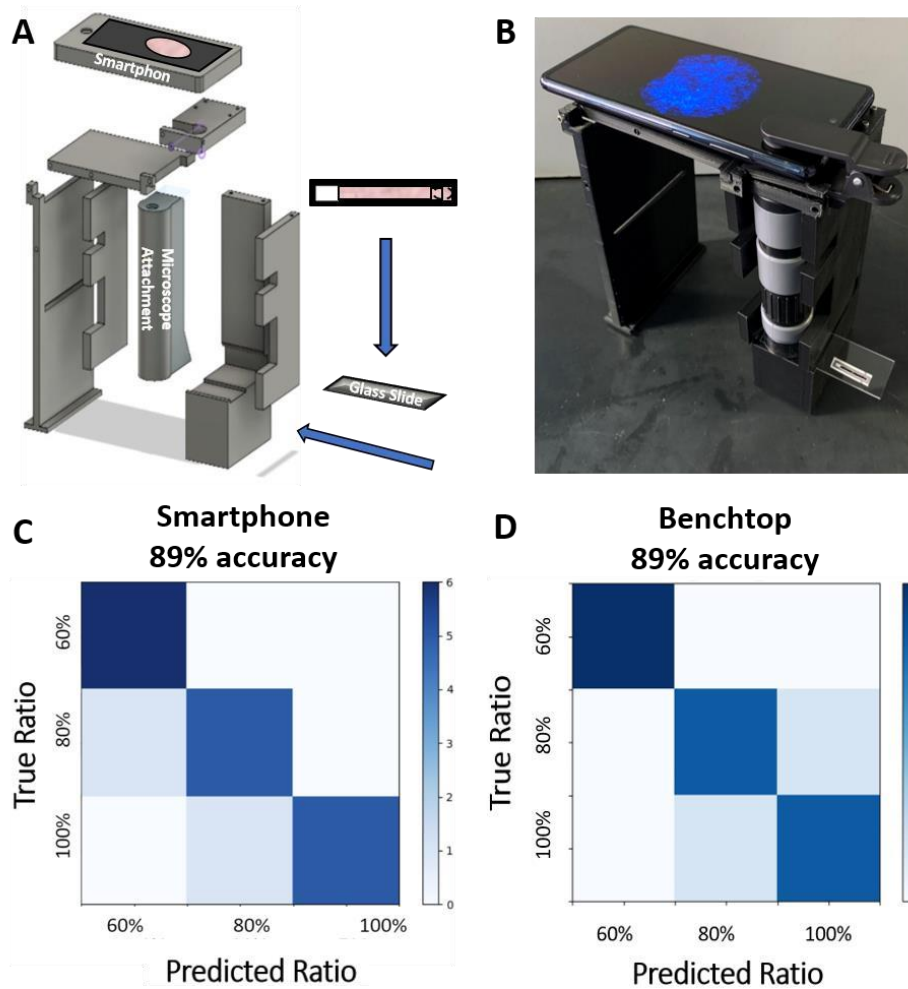


Figure A-6. Machine learning cell chromatography results on both microscope platforms. A) Schematic representation of the smartphone-based fluorescence microscope image system used for cell chromatography in expanded CAD view. B) Image of smartphone microscope housing with example image displayed. C) Confusion matrix from the final smartphone microscopebased model, indicating a model accuracy of 89%. Whole data set is available in Supplementary Table S2. Processed fluorescence images are summarized in Supplementary Figure S4. D) Confusion matrix from the final benchtop microscope-based model, indicating a model accuracy of 89%. Whole data set is available in Supplementary Table S1.

After taking microscope images along the flow lanes of 18 chips (6 for each bright:dim ratio), the microscope images were fed into the microscope image analysis and machine learning algorithms, where the overall model performance was calculated. The dataset used for machine learning model creation consisted of a total of 18 observations, each with 10 features (2 features for all 5 images). The whole data set is available in Supplementary Table S2. After optimizing the smartphone-based platform, the best overall model used support vector machine algorithms and had an accuracy of 89%, and the corresponding confusion matrix can be found in Figure 6C. Analysis algorithms were uploaded and run on a cloud (Google Colab folder) that allowed the end-user to conduct image and video analyses on the same phone that they used to acquire the data in the first place.

This accuracy of 89% rivals that of a flow cytometry. For example, Duong et al. reported the clinical sensitivity and specificity of 99.5% and 80.6% for counting the white blood cells from the urine samples from urinary tract infection (UTI) patients [29]. While clinical accuracy has not been reported, we can expect the clinical accuracy being somewhere in between 99.5% and 80.6%, which is equivalent to 89% demonstrated in this work. Savage et al. reported the clinical accuracy, sensitivity, and specificity for the flow cytometry analysis of lymphoid from the fine needle aspiration samples, 88.4%, 85.8%, and 92.9%, respectively, also equivalent to 89% of this work [30]. It should be noted that the buffy coat blood samples used in this work are more complex than the urine samples or the fine needle aspiration lymphoid samples. In addition, subpopulation of cells was not evaluated in these works, potentially indicating the superiority of this work. Petrunkina and Harrison has also reported the issue of systematic misestimation of cell subpopulations by a flow cytometry [31].

Conclusions

In this work, we have developed a paper-based microfluidic chip with two main zones, capable of quantifying cytokine (IL-2) and NK cell through flow-based measurements taken by a smartphone, as well as the NK cell CD56 subpopulations via smartphone-based fluorescence microscopic analysis and machine learning-based classification. This quantification was performed with samples diluted in a complex, clinically relevant buffy coat blood sample. After extracting characteristic K values from the flow velocity profiles from the parsed flow videos, very low limits of detection were demonstrated, 98 IU/mL for cytokine IL-2 and 68 cells/mL NK cell. Machine learning classification accuracy for the cell chromatography lane was found to be 89% on the smartphone-based device, rivaling the accuracy of 89% (note: these values are accidental coincidences) on the conventional benchtop microscope and the clinical accuracies of 86%-93% of flow cytometry. By applying a cell chromatographic separation as demonstrated in this paper, we have overcome limitations in traditional cell chromatography that is unable to separate subpopulations of the same cell type by taking advantage of machine learning classification to categorize samples from inherently noisy fluorescent images. On-device analysis was also demonstrated with the cloud-based analysis using Google Colab, which is not possible with a simple CCD or CMOS camera. Overall, our device requires simple sample processing steps to perform this assay in under 10 min. In contrast to the more accurate, but also costlier and less accessible flow cytometry standard methods of cell subpopulation quantification, our paper based microfluidic platform provides a cost effective and easy to use alternative that can process more complex, dirty samples to quantify desired components. Future work should include the application of this novel device towards monitoring and prognostics of NK cell-based therapy, providing more clinical accessibility, and addressing patient-to-patient and smartphone-to-smartphone variations.

Acknowledgements

The authors would like to acknowledge Samuel Kim for his help in the process of this work. This work was supported by the Cardiovascular Biomedical Engineering Training Grant from National Heart, Lung, and Blood Institute of the U.S. National Institutes of Health, grant number T32HL007955, awarded to A.S.D. and J.-Y.Y. This work was also supported by National Heart, Lung, and Blood Institute of the U.S. National Institutes of Health, grant number R01HL138242, awarded to Y.-W.W.

References

- [1] Yilmaz, A., Cui, H., Caligiuri, M.A., Yu, J., 2020. Chimeric antigen receptor-engineered natural killer cells for cancer immunotherapy. *Journal of Hematology & Oncology* 13, 168. <https://doi.org/10.1186/s13045-020-00998-9>
- [2] Wu, S.-Y., Fu, T., Jiang, Y.-Z., Shao, Z.-M., 2020. Natural killer cells in cancer biology and therapy. *Molecular Cancer* 19, 120. <https://doi.org/10.1186/s12943-020-01238-x>
- [3] Poli, A., Michel, T., Thérésine, M., Andrès, E., Hentges, F., Zimmer, J., 2009. CD56^{bright} natural killer (NK) cells: an important NK cell subset. *Immunology* 126(4), 458-465. <https://doi.org/10.1111/j.1365-2567.2008.03027.x>
- [4] Mandal, A., Viswanathan, C., 2015. Natural killer cells: In health and disease. *Hematology/Oncology and Stem Cell Therapy* 8(2), 47-55. <https://doi.org/10.1016/j.hemonc.2014.11.006>
- [5] Pedersen, B.K., Tvede, N., Hansen, F.R., Andersen, V., Bendix, T., Bendixen, G., Bendtzen, K., Galbo, H., Haahr, P.M., Klarlund, K., Sylvest, J., Thomsen, B.S., Halkjaer-Kristensen J., 1988. Modulation of natural killer cell activity in peripheral blood by physical exercise. *Scandinavian Journal of Immunology* 27(6), 673-678. <https://doi.org/10.1111/j.1365-3083.1988.tb02400.x>
- [6] Merino, A., Zhang, B., Dougherty, P., Luo, X., Wang, J., Blazar, B.R., Miller, J.S., Cichocki, F., 2019. Chronic stimulation drives human NK cell dysfunction and epigenetic reprogramming. *Journal of Clinical Investigation* 129(9), 3770-3785. <https://doi.org/10.1172/JCI125916>
- [7] Ming, B., Wu, T., Cai, S., Hu, P., Tang, J., Zheng, F., Ye, C., Dong, L., 2020. The Increased

Ratio of Blood CD56^{bright} NK to CD56^{dim} NK Is a Distinguishing Feature of Primary Sjögren's Syndrome. *Journal of Immunology Research* 2020, 7523914.

<https://doi.org/10.1155/2020/7523914>

- [8] Michel, T., Poli, A., Cuapio, A., Briquemont, B., Iserentant, G., Ollert, M., Zimmer, J., 2016.

Human CD56 “bright” NK Cells: An Update. *The Journal of Immunology* 196(7), 2923-2931. <https://doi.org/10.4049/jimmunol.1502570>

- [9] Vujanovic, L., Chuckran, C., Lin, Y., Ding, F., Sander, C.A., Santos, P.M., Lohr, J., Mashadi-Hosseini, A., Warren, S., White, A., Huang, A., Kirkwood, J.M., Butterfield, L.H., 2019. CD56^{dim} CD16⁻ Natural Killer Cell Profiling in Melanoma Patients Receiving a Cancer Vaccine and Interferon- α . *Frontiers in Immunology* 10, 14.

<https://doi.org/10.3389/fimmu.2019.00014>

- [10] Ruggeri, L., 2002. Effectiveness of donor natural killer cell alloreactivity in mismatched hematopoietic transplants. *Science* 295(5562), 2097-2100.

<https://doi.org/10.1126/science.1068440>

- [11] Bonifant, C.L., Jackson, H.J., Brentjens, R.J., Curran, K.J., 2016. Toxicity and management in CAR T-cell therapy. *Molecular Therapy - Oncolytics* 3,1601.

<https://doi.org/10.1038/mto.2016.11>

- [12] Ben-Shmuel, A., Biber, G., Barda-Saad, M., 2020. Unleashing Natural Killer Cells in the Tumor Microenvironment—The Next Generation of Immunotherapy? *Frontiers in Immunology* 11, 275. <https://doi.org/10.3389/fimmu.2020.00275>

- [13] Olson, J.A., Leveson-Gower, D.B., Gill, S., Baker, J., Beilhack, A., Negrin, R.S., 2010. NK cells mediate reduction of GVHD by inhibiting activated, alloreactive T cells while

- retaining GVT effects. *Blood* 115(21), 4293-4301. <https://doi.org/10.1182/blood-2009-05-222190>
- [14] Bryceson, Y.T., Fauriat, C., Nunes, J.M., Wood, S.M., Björkström, N.K., Long, E.O., Ljunggren, H.-G., 2010. Functional Analysis of Human NK Cells by Flow Cytometry. In: Campbell, K. (ed.) *Natural Killer Cell Protocols. Methods in Molecular Biology (Methods and Protocols)*, vol. 612, pp. 335-352. https://doi.org/10.1007/978-1-60761-362-6_23
- [15] Cooper, M.A., Caligiuri, M.A., 2004. Isolation and Characterization of Human Natural Killer Cell Subsets. *Current Protocols in Immunology* 60, 7.34.1–12
<https://doi.org/10.1002/0471142735.im0734s60>
- [16] Shrirao, A.B., Fritz, Z., Novik, E.M., Yarmush, G.M., Schloss, R.S., Zahn, J.D., Yarmush, M.L., 2018. Microfluidic flow cytometry: The role of microfabrication methodologies, performance and functional specification. *Technology* 6(1), 1-23.
<https://doi.org/10.1142/S2339547818300019>
- [17] İçöz, K., Eken, A., Çınar, S., Murat, A., Özcan, S., Ünal, E., Deniz, G., 2020. Immunomagnetic separation of B type acute lymphoblastic leukemia cells from bone marrow with flow cytometry validation and microfluidic chip measurements. *Separation Science and Technology*. doi: 10.1080/01496395.2020.1835983.
<https://doi.org/10.1080/01496395.2020.1835983>
- [18] Klug, K.E., Reynolds, K.A., Yoon, J.-Y., 2018. A Capillary Flow Dynamics-Based Sensing Modality for Direct Environmental Pathogen Monitoring. *Chemistry - A European Journal* 24(23), 6025-6029. <https://doi.org/10.1002/chem.201800085>
- [19] Chung, S., Breshears, L.E., Gonzales, A., Jennings, C.M., Morrison, C.M., Betancourt,

- W.Q., Reynolds, K.A., Yoon, J.-Y., 2021. Norovirus Detection in Water Samples at the Level of Single Virus Copies per Microliter Using a Smartphone-based Fluorescence Microscope. *Nature Protocols*, 16(3), 1452-1475. <https://doi.org/10.1038/s41596-020-00460-7>
- [20] Ulep, T.-H., Yoon, J.-Y. 2018. Challenges in paper-based fluorogenic optical sensing with smartphones. *Nano Convergence* 5, 14. <https://doi.org/10.1186/s40580-018-0146-1>
- [21] Ulep, T.-H., Zenhausem, R., Gonzales, A., Knoff, D.S., Lengerke Diaz, P.A., Castro, J.E., Yoon, J.-Y., 2020. Smartphone based on-chip fluorescence imaging and capillary flow velocity measurement for detecting ROR1+ cancer cells from buffy coat blood samples on dual-layer paper microfluidic chip. *Biosensors and Bioelectronics* 153, 112042. <https://doi.org/10.1016/j.bios.2020.112042>
- [22] Chung, S., Breshears, L.E., Perea, S., Morrison, C.M., Betancourt, W.Q., Reynolds, K.A., Yoon, J.-Y., 2019. Smartphone-Based Paper Microfluidic Particulometry of Norovirus from Environmental Water Samples at the Single Copy Level. *ACS Omega* 4(6), 11180-11188. <https://doi.org/10.1021/acsomega.9b00772>
- [23] Mohr, F., Przibilla, S., Leonhardt, F., Stemberger, C., Dreher, S., Müller, T.R., Fräßle, S.P., Schmidt, G.P., Kiene, M.-L., Stadler, H., Busch, D.H., 2018. Efficient immunoaffinity chromatography of lymphocytes directly from whole blood. *Scientific Reports* 8, 16731. <https://doi.org/10.1038/s41598-018-34589-z>
- [24] Molday, R.S., Dreyer, W.J., Rembaum, A., Yen, S.P., 1975. New immunolates: visual markers of antigens on lymphocytes for scanning electron microscopy. *Journal of Cell Biology* 64(1), 75-88. <https://doi.org/10.1083/jcb.64.1.75>

- [25] Somanchi, S.S., Senyukov, V.V., Denman, C.J., Lee, D.A. 2011. Expansion, purification, and functional assessment of human peripheral blood NK cells. *Journal of Visualized Experiments* 48, e2540. <https://doi.org/10.3791/2540>
- [26] Chen, J.S., Chen, P.F., Lin, H.T.H., Huang, N.T., 2020. A Localized surface plasmon resonance (LSPR) sensor integrated automated microfluidic system for multiplex inflammatory biomarker detection. *Analyst*, 145(23), pp.7654-7661.
<https://doi.org/10.1039/D0AN01201G>
- [27] Park, K.H., Park, H., Kim, M., Kim, Y., Han, K. and Oh, E.J., 2013. Evaluation of NK cell function by flowcytometric measurement and impedance based assay using real-time cell electronic sensing system. *BioMed Research International*, 2013, 210726.
<https://doi.org/10.1155/2013/210726>
- [28] Zhu, J., Wang, X., Xu, X., Abassi, Y.A., 2006. Dynamic and label-free monitoring of natural killer cell cytotoxic activity using electronic cell sensor arrays. *Journal of Immunological Methods*, 309(1-2), 25-33. <https://doi.org/10.1016/j.jim.2005.10.018>
- [29] Duong, H.P., Wissing, K.M., Tram, N., Mascart, G., Lepage, P., Ismaili, K., 2016. Accuracy of automated flow cytometry-based leukocyte counts to rule out urinary tract infection in febrile children: A prospective cross-sectional study. *Journal of Clinical Microbiology* 54(12), 2975-2981. <https://doi.org/10.1128/JCM.01382-16>
- [30] Savage, E.C., Vanderheyden, A.D., Bell, A.M., Syrbu, S.I., Jensen, C.S., 2011. Independent diagnostic accuracy of flow cytometry obtained from fine-needle aspirates: A 10-year experience with 451 cases. *American Journal of Clinical Pathology* 135, 304-309. <https://doi.org/10.1309/AJCPHY69XVJGULKO>

Supplementary

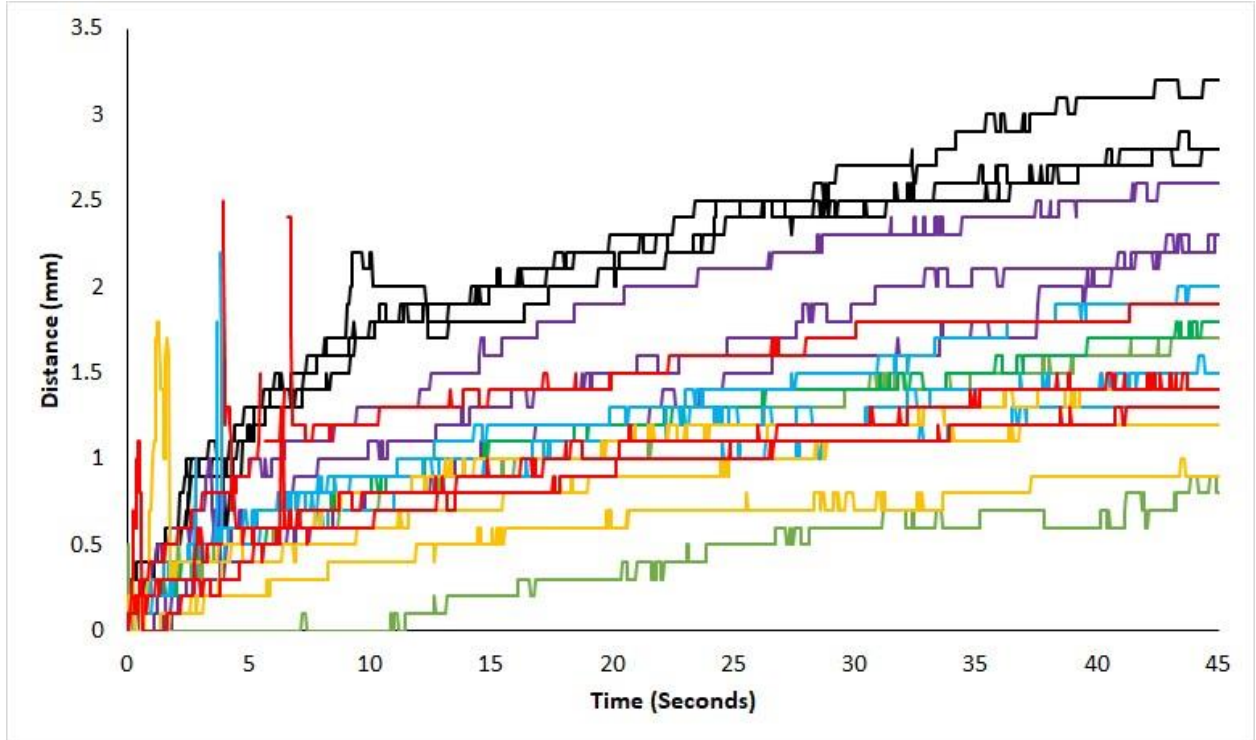


Figure A-S1. d (flow distance, mm) vs. t (time, s) plots for assaying IL-2. Black lines indicate NTC, purple indicates 50 IU/mL IL-2, green indicates 100 IU/mL, blue indicates 15 IU/mL, orange indicates 200 IU/mL, and red indicates 250 IU/mL.

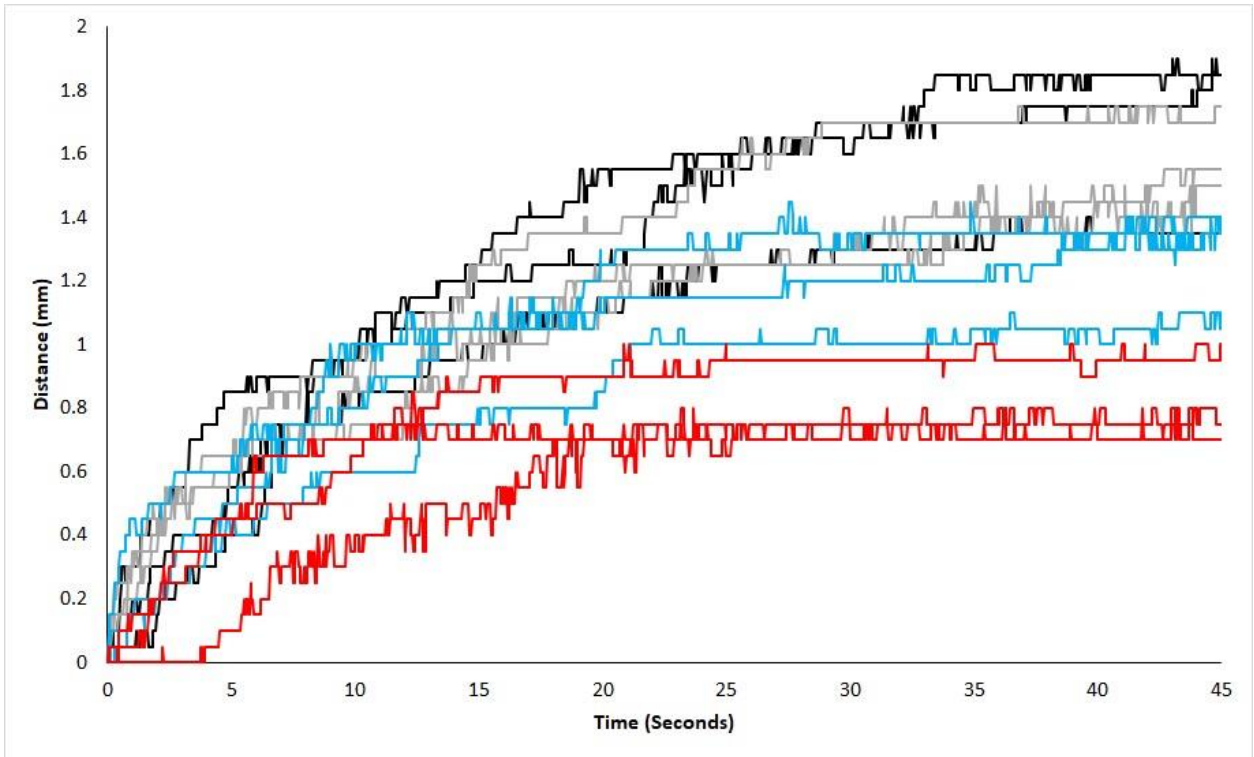
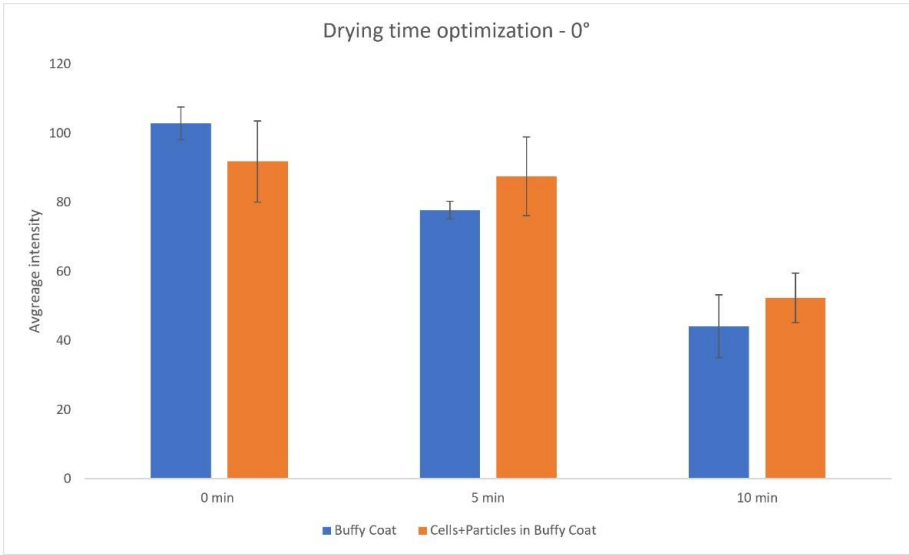


Figure A-S2. d (flow distance, mm) vs. t (time, s) plots for assaying NK-92. Black lines indicate NTC, grey indicates 102 NK cells/mL, blue indicates 103 NK cells/mL, and red indicates 104 NK cells/mL.



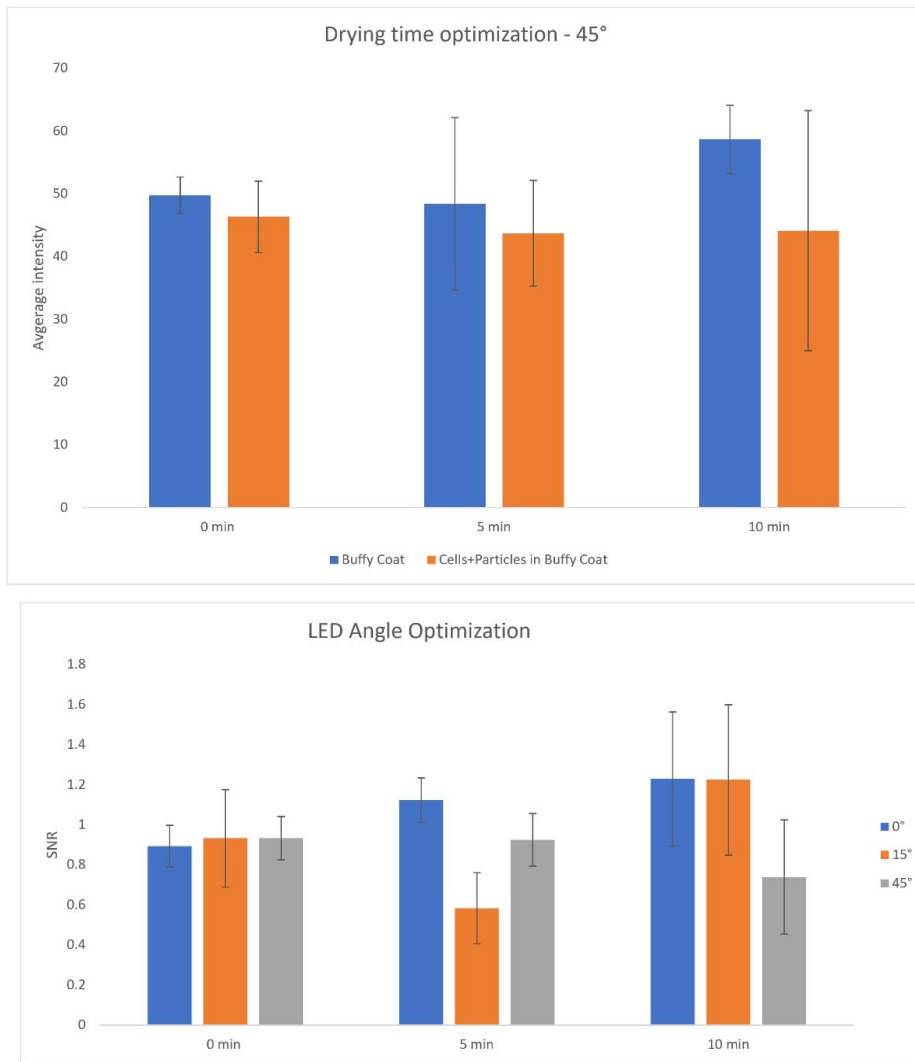


Figure A-S3. Optimization of drying time and LED angle.

100% CD56^{dim} : 0% CD56^{bright}

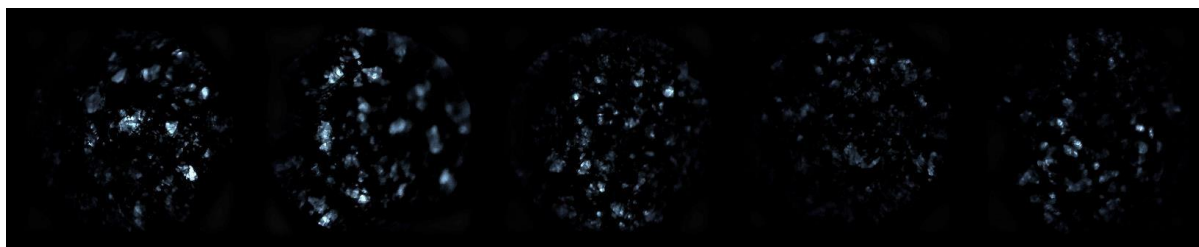
Chip 1: FOV_1

FOV_2

FOV_3

FOV_4

FOV_5



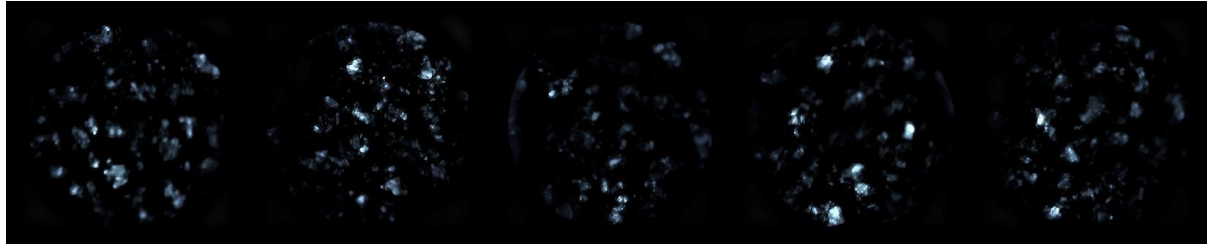
Chip 3: FOV_1

FOV_2

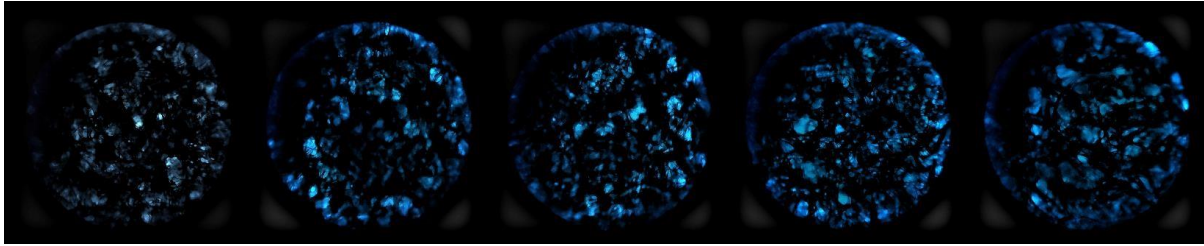
FOV_3

FOV_4

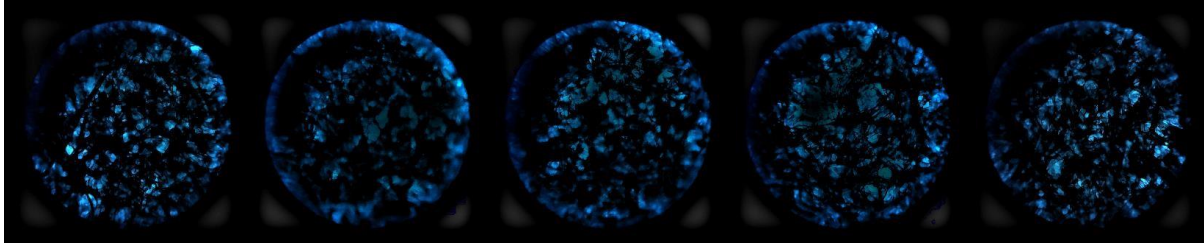
FOV_5



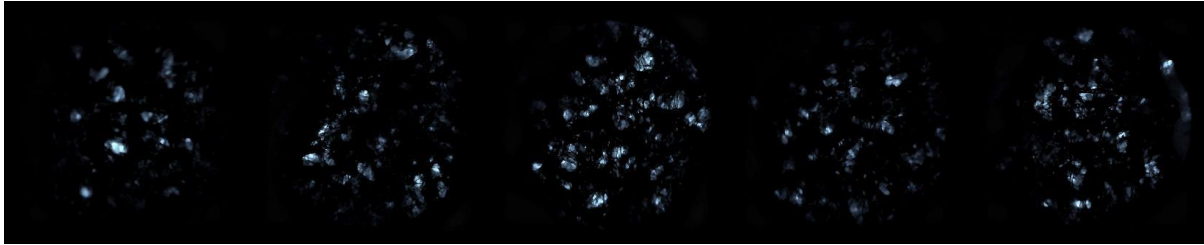
Chip 4: FOV_1 FOV_2 FOV_3 FOV_4 FOV_5



Chip 5: FOV_1 FOV_2 FOV_3 FOV_4 FOV_5

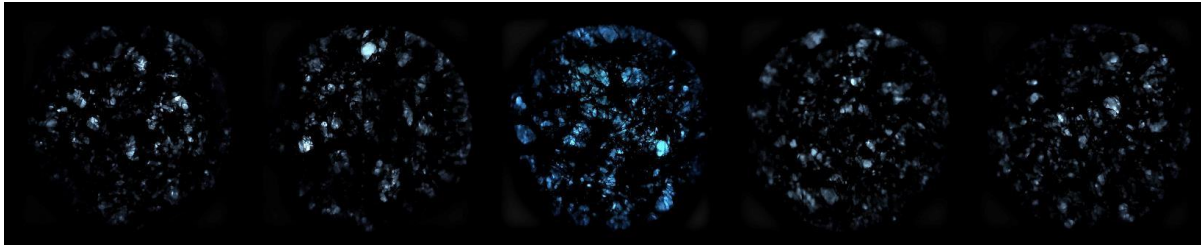


Chip 6: FOV_1 FOV_2 FOV_3 FOV_4 FOV_5



80% CD56^{dim} : 20% CD56^{bright}

Chip 1:



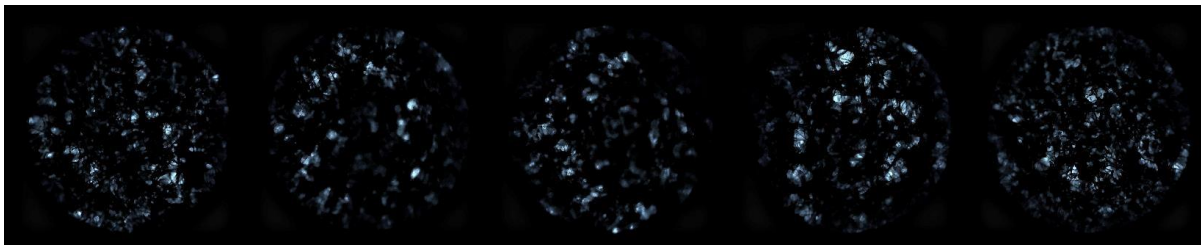
Chip 2: FOV_1

FOV_2

FOV_3

FOV_4

FOV_5



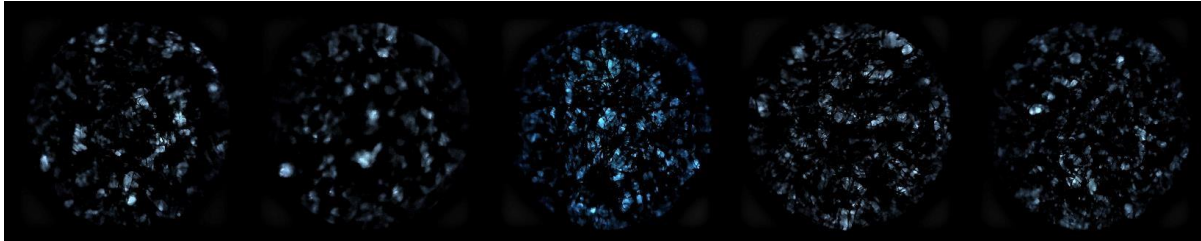
Chip 3: FOV_1

FOV_2

FOV_3

FOV_4

FOV_5



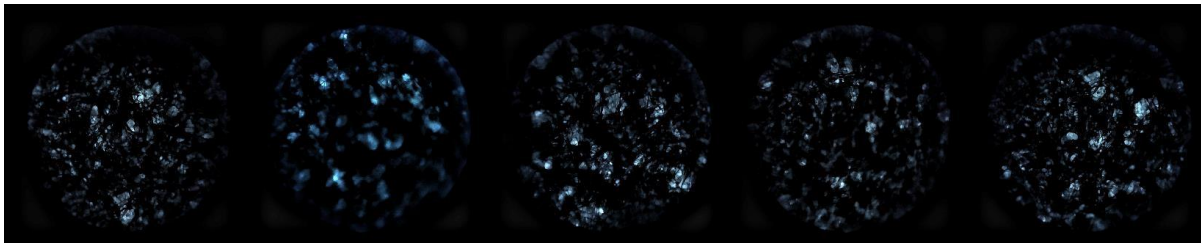
Chip 4: FOV_1

FOV_2

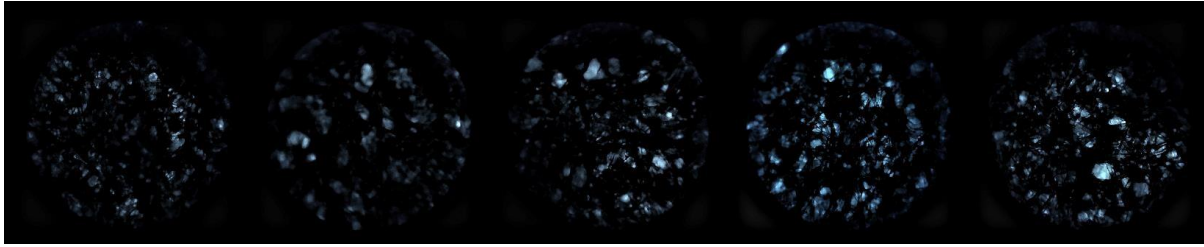
FOV_3

FOV_4

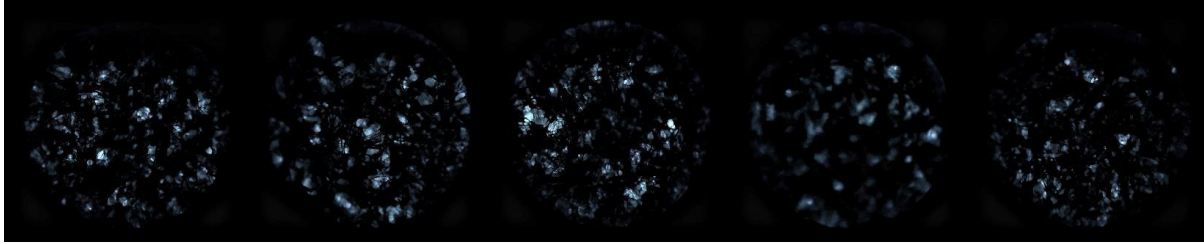
FOV_5



Chip 5:

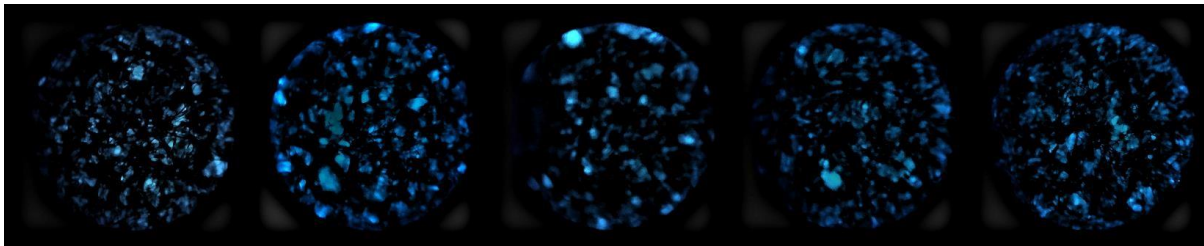


Chip 6: FOV_1 FOV_2 FOV_3 FOV_4 FOV_5

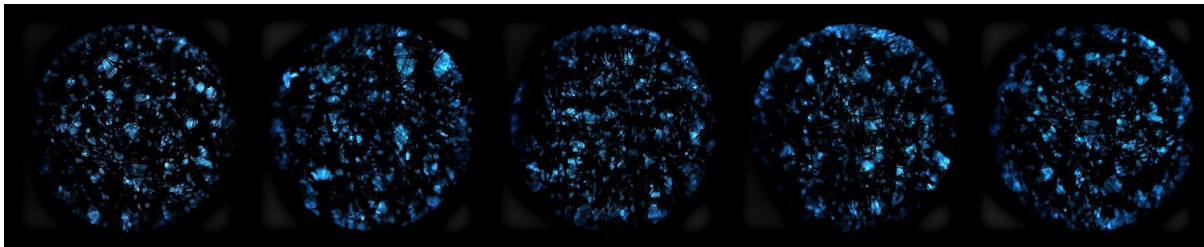


60% CD56dim:40% CD56bright

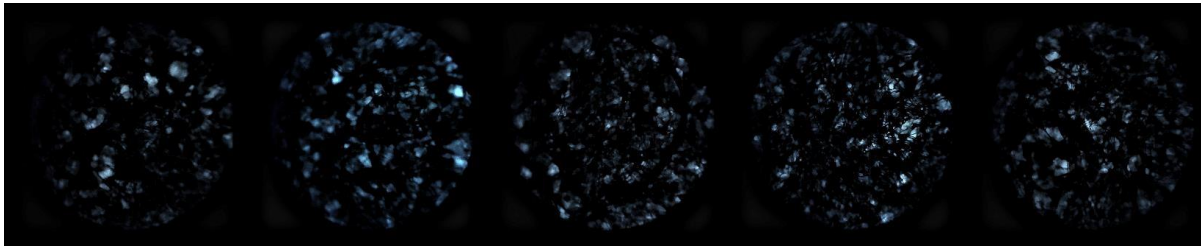
Chip 1: FOV_1 FOV_2 FOV_3 FOV_4 FOV_5



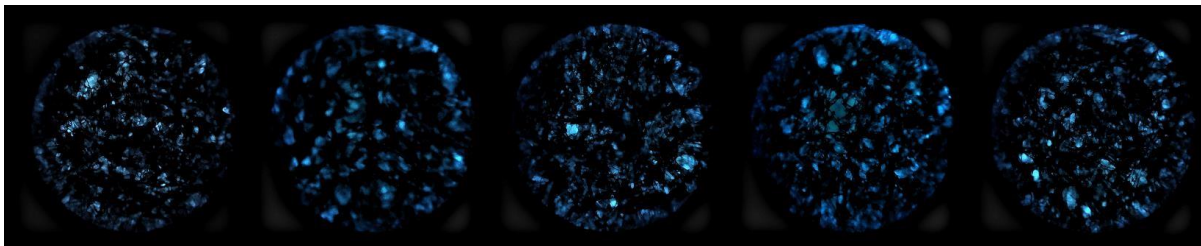
Chip 2: FOV_1 FOV_2 FOV_3 FOV_4 FOV_5



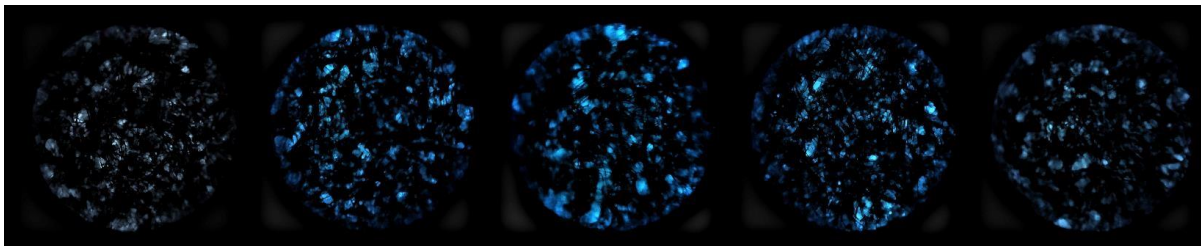
Chip 3: : FOV_1 FOV_2 FOV_3 FOV_4 FOV_5



Chip 4: FOV_1 FOV_2 FOV_3 FOV_4 FOV_5



Chip 5 FOV_1 FOV_2 FOV_3 FOV_4 FOV_5



Chip 6: FOV_1 FOV_2 FOV_3 FOV_4 FOV_5

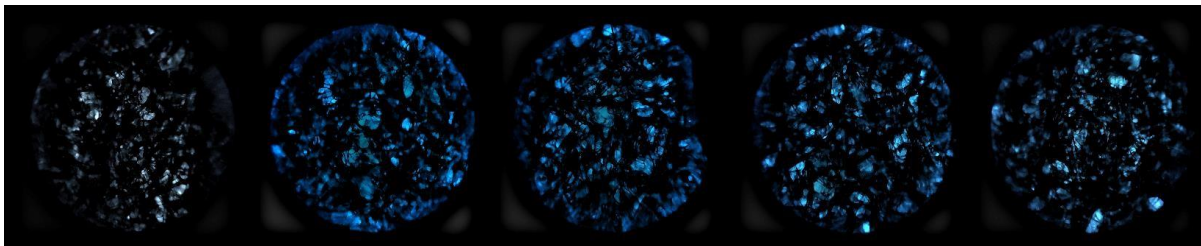


Figure A-S4. Adjusted smartphone fluorescence microscope images.

Table A-S1. All benchtop machine learning data.

Chip	Class	Scipy 1	Manual Count 1	# Bound 1	% Bound 1	Scipy 2	Manual Count 2	# Bound 2	% Bound 2
100% Dim_1	3	13	34	7	20.6	9	26	3	11.5
100% Dim_2	3	2	2	0	0	10	23	0	0
100% Dim_3	3	15	32	8	25	22	44	3	6.8
100% Dim_4	3	29	60	29	48.3	10	23	6	26.1
100% Dim_5	3	18	32	6	18.8	11	20	5	25
100% Dim_6	3	68	143	29	20.3	83	250	67	26.8
80% Dim_1	2	10	20	0	0	12	28	2	7.1
80% Dim_2	2	50	133	46	34.6	114	278	115	41.4
80% Dim_3	2	166	424	164	38.7	201	461	168	36.4
80% Dim_4	2	107	219	67	30.6	178	409	153	37.4
80% Dim_5	2	112	266	71	26.7	138	292	87	29.8
80% Dim_6	2	223	571	238	41.7	200	537	220	41
60% Dim_1	1	51	123	53	43.1	142	363	137	37.7
60% Dim_2	1	101	256	51	19.9	90	229	42	18.3
60% Dim_3	1	279	642	222	34.6	200	501	155	30.9
60% Dim_4	1	45	113	0	0	97	200	24	12
60% Dim_5	1	183	468	145	31	179	442	155	35.1
60% Dim_6	1	230	529	173	32.7	188	420	145	34.5

Scipy 3	Manual Count 3	# Bound 3	% Bound 3	Scipy 4	Manual Count 4	# Bound 4	% Bound 4
24	55	9	16.4	11	50	45	90
11	19	3	15.8	14	27	0	0
20	51	16	31.4	15	34	0	0
17	40	0	0	19	41	19	46.3
23	65	10	15.4	15	35	3	8.6
41	100	24	24	22	57	10	17.5
8	29	0	0	10	23	2	8.7
57	120	15	12.5	67	134	47	35.1
104	259	74	28.6	24	69	16	23.2
136	334	94	28.1	40	78	22	28.2
120	316	116	36.7	135	389	154	39.6
152	333	89	26.7	32	92	51	55.4
59	148	25	16.9	98	292	176	60.3
111	249	77	30.9	118	273	76	27.8
219	519	212	40.8	213	489	145	29.7
136	324	66	20.4	131	382	186	48.7
196	526	244	46.4	123	288	102	35.4
239	577	210	36.4	267	695	356	51.2

Scipy 5	Manual Count 5	# Bound 5	% Bound 5	Scipy 6	Manual Count 6	# Bound 6	% Bound 6
6	13	0	0	9	22	5	22.7
17	44	0	0	7	8	0	0
16	43	20	46.5	13	24	2	8.3
13	25	11	44	10	25	7	28
19	40	10	25	1	2	0	0
36	89	47	52.8	21	69	39	56.5
9	13	0	0	12	40	23	57.5
15	26	0	0	50	138	56	40.6
50	102	28	27.5	50	113	35	31
27	77	25	32.5	47	146	81	55.5
38	80	12	15	45	127	51	40.2
49	122	40	32.8	22	42	6	14.3
107	225	110	48.9	0	0	0	0
5	12	0	0	30	65	2	3.1
85	195	63	32.3	0	0	0	0
24	55	17	30.9	33	76	11	14.5
323	787	304	38.6	27	61	9	14.8
370	799	302	37.8	5	6	2	33.3

Table A-S2. All smartphone machine learning data.

Chip	Class	Scipy 1	Manual Count 1	Scipy 2	Manual Count 2
100% Dim_1	3	1225	1374510	1956	1338782
100% Dim_2	3	2195	1303717	3032	1253682
100% Dim_3	3	2305	1266923	1769	1346978
100% Dim_4	3	511	1474962	521	1471069
100% Dim_5	3	1005	1510777	744	1493254
100% Dim_6	3	2801	1269940	2459	1214530
60% Dim_1	1	400	1483679	983	1451673
60% Dim_2	1	426	1478665	421	1474628
60% Dim_3	1	421	1464872	417	1462260
60% Dim_4	1	390	1476266	465	1469844
60% Dim_5	1	371	1473238	460	1478979
60% Dim_6	1	489	1490926	759	1450543
80% Dim_1	2	811	1404557	515	1436701
80% Dim_2	2	428	1444817	684	1426223
80% Dim_3	2	391	1450003	418	1453855
80% Dim_4	2	288	1453546	427	1447171
80% Dim_5	2	332	1452558	471	1438972
80% Dim_6	2	551	1439717	379	1447450

Scipy 3	Manual Count 3	Scipy 4	Manual Count 4	Scipy 5	Manual Count 5
2812	1294316	3196	1235564	3026	1250588
2697	1241639	3047	1276360	2835	1282283
1103	1410754	1866	1342631	1232	1391812
635	1486582	562	1476431	1492	1431320
728	1490954	391	1476142	664	1473878
2931	1198789	2368	1236156	4274	1148723
499	1461052	414	1477041	488	1467697
608	1462499	445	1478489	378	1470588
361	1467305	368	1458402	481	1448001
455	1471735	433	1477565	368	1470953
409	1476024	375	1472859	340	1469901
476	1478932	379	1471393	406	1466359
436	1445218	437	1437151	902	1402277
666	1425176	353	1458323	445	1446745
350	1465531	413	1450579	394	1454312
421	1445807	398	1450260	740	1435045
370	1464340	867	1426398	1153	1405156
312	1452363	975	1412879	1478	1384491

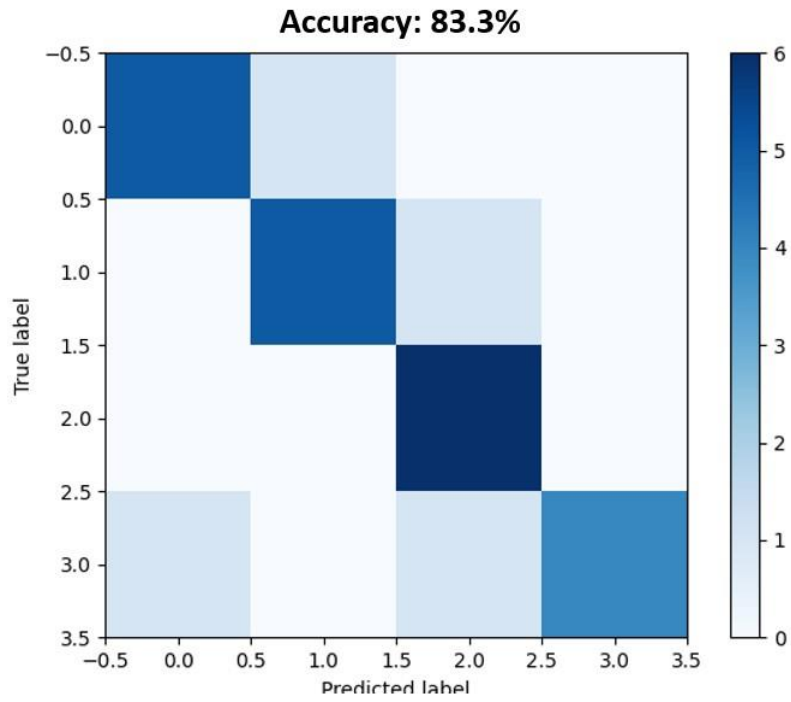


Figure A-S5: Confusion matrix depicting 4-class classification using the platform described in this study

**APPENDIX B: SMARTPHONE-BASED AUTOFLUORESCENCE IMAGING TO
DETECT BACTERIAL SPECIES ON LABORATORY SURFACES**

Bailey C. Buchanan^{1†}, Babak Safavinia^{1†}, Lillian Wu¹, and Jeong-Yeol Yoon^{1,*}

¹Department of Biomedical Engineering, The University of Arizona, Tucson, Arizona 85721,
United States

[†]These authors contributed equally to this work

*Corresponding author, E-mail: jyyoon@arizona.edu

In revision

Abstract

The potential of bacterial contamination is commonly seen in biological and clinical laboratory surfaces, creating a need to detect the presence of bacteria on a surface. Various bacterial species have been found to naturally exist on surfaces, including *Escherichia coli*, *Salmonella* Typhimurium, and *Staphylococcus aureus* that were investigated in this study. Bacterial presence was identified from laboratory surfaces using a smartphone and low-cost components without culturing or staining. Autofluorescence from bacteria was quantified using a 405 nm LED as an excitation light source. A low-cost acrylic film could isolate the autofluorescence emission. ImageJ was used to process and analyze the images and quantify the emitted autofluorescence signal. This imaging platform successfully detected the presence of all three bacterial species from the heavily used laboratory surfaces. An exponentially decreasing trend was observed with decreasing bacterial concentration, and the limit of detection was 10^4 CFU/cm². It could also distinguish from tap water, protein (bovine serum albumin), and NaCl solutions. This preliminary work emphasizes the ability to detect autofluorescence signals of bacteria and non-microbial surface contaminants using a cost-effective and straightforward imaging platform.

Introduction

Bacterial species are commonly used or found in biological and clinical laboratory settings, leading to the potential of bacterial contamination. Laboratory experiments and clinical diagnoses may be influenced by bacterial contamination, which would lead to erroneous measurements and inaccurate results [18]. Therefore, there is a need to detect bacterial presence on laboratory and clinical surfaces.

Bacterial contamination can stem from various bacterial species that have been found to commonly exist on surfaces, including *Escherichia coli*, *Salmonella enterica* (including serovar Typhimurium), and *Staphylococcus aureus* [2], [3]. It has been reported that *S. aureus* can survive well on many different surfaces [2], [4]. In addition, *E. coli* was found to be one of the top five bacterial species on an anatomical model in a laboratory setting³ and exhibiting strong attachment to abiotic surfaces [5]. All of these indicate that several bacterial species can survive on surfaces in a laboratory environment. Therefore, a rapid and low-cost bacterial detection method is needed to ensure that a laboratory surface is free of bacterial contamination.

Bacteria on laboratory surfaces have traditionally been identified and quantified by swabbing the surface, dissolving into a solution, and culturing them on selective or differential media [6]. Colonies are counted visually to quantify their amounts. While this method is low-cost and straightforward, it requires an overnight culture to see the results. Nucleic acid amplification techniques, most notably polymerase chain reaction (PCR), have also been popularly used, reducing the assay time to several hours. However, it requires specialized equipment such as a thermal cycler and a gel electrophoresis system (alternatively a real-time thermal cycler) and highly trained personnel to extract the gene and operate such equipment [7]. Antibody-based biosensors, typically incorporated on paper strips or microfluidic devices, have also popularly

been investigated for bacterial detection [8]. However, they still require swab-sampling and manual loading onto the platforms. All of the above methods require sampling, manual sampling loading, and material preparations (media, PCR kits, antibodies, etc.). If we can detect the bacterial presence directly from the surface with neither sampling nor staining, it will provide a rapid and straightforward bacterial detection method from laboratory surfaces. In addition, it will be beneficial if we can also use a smartphone (specifically a smartphone camera) as an optical reader device, which has been widely investigated for numerous biosensing and medical diagnostics applications [9].

This work aims to detect autofluorescence from bacteria using a smartphone camera and low-cost components (a light-emitting diode and an acrylic film) towards low-cost and straightforward bacteria detection from laboratory surfaces. Intrinsic fluorescence (autofluorescence) can be generated from bacterial species' cellular constituents, such as tryptophan in proteins, nucleic acids, and lipofuscins, and especially porphyrins [10], [11]. Such autofluorescence allows for the detection of bacteria without fluorescence staining [12]–[15].

In this study, a bacterial autofluorescence imaging setup was created to detect surface-level bacterial contaminants. A smartphone platform was used to image a laboratory surface, utilizing the smartphone's advantages of being cost-effective and easy to image [16], [17]. A single 405 nm light-emitting diode (LED) was used as a fluorescence excitation light source, and an acrylic film was used as a low-cost optical bandpass filter. A 405 nm LED was chosen due to its ability to excite bacterial species [18]–[20]. More specifically porphyrins produced by bacteria are commonly used as a fluorescent biomarker that gets optimally excited by the 405nm LED [21], [22]. Indeed, the 405 nm excitation generated fluorescence emissions from all three bacterial species, while it did not induce significant autofluorescence from other fluorescing

controls, including tap water, salt solution, and protein solution. This study aimed to create a smartphone platform that can detect bacterial species without fluorescence staining. This imaging setup can potentially be applied in the future to scan surfaces and identify bacterial presence on that surface. This practice can then limit the bacterial contamination found on the surfaces in laboratory and clinical settings.

Materials and methods

Bacteria culture

Three bacteria species were examined, including *Escherichia coli* K12 lyophilized powder (Sigma, St. Louis, MO, USA), *Salmonella enterica* serovar Typhimurium Z005 strain (ZeptoMetrix, Buffalo, NY, USA), and methicillin-susceptible *Staphylococcus aureus* (MSSA, ZeptoMetrix, Buffalo, NY, USA). *E. coli* was cultured by first adding 10 mL of lysogeny broth (LB) to a 15-mL centrifuge tube. Next, a small scoop of about 1 µg of *E. coli* powder was added to the LB and mixed. The centrifuge tube was loosely sealed and then parafilmmed on the cap. This tube was incubated for 24 hr at 37°C. The same procedure was completed to culture *S. Typhimurium* and *S. aureus*.

The concentration of each species was validated using a spectrophotometer. The intensity value of a blank cuvette of 1 mL of DI water was measured first and was recorded. DI water was chosen as the control because when the samples were diluted the majority of the solution consisted of DI water. In addition, the final set of experiments consisted of removal of LB and resuspension of the bacteria in DI water. Following this, the intensity value of a diluted sample of the bacteria species was measured. The diluted sample consisted of 900 µL of LB, since this is the growth medium used for each bacteria species, and 100 µL of the cultured bacteria. The optical density (OD) value at 600 nm was obtained from the miniature spectrophotometer (USB4000; Ocean Optics, Dunedin, FL, USA) of each sample to obtain the initial concentration of each bacterium. Then serial dilutions were completed to obtain bacteria concentrations of 10^7 CFU/mL to 10^4 CFU/mL.

A 10 µL drop was placed onto a surface (microscope slide or laboratory desk), and then the placed droplet was measured to be about 1 cm². A conversion was made to determine the

surface concentration (CFU/cm²) from the volumetric concentration (CFU/mL). Since 10 μ L created 1 cm² surface, 10⁸ CFU/mL became equivalent to 10⁶ CFU/cm².

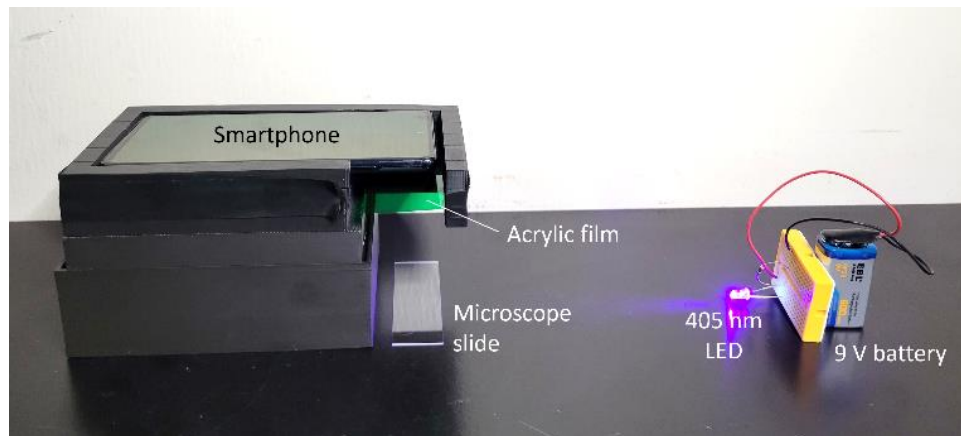


Fig B-1. Bacteria autofluorescence imaging set up on a laboratory desk. Acrylic film (as a low-cost optical bandpass filter) is placed in front of the Samsung S20 camera to isolate the autofluorescence signal. A 405 nm LED is used to excite the bacteria droplet from the side. 10 μ L bacterial droplets are added on a microscope slide (shown in the figure) or directly on a laboratory desk surface.

Imaging procedure

Acrylic film (#389; Color Filter Booklet; Edmund Optics, AZ, USA) was used as a low-cost optical bandpass filter, allowing only the wavelengths from 480 to 520 nm to pass through. The acrylic film was placed in front of the smartphone camera. The specific acrylic film was chosen after trial and error to be the optimal filter for isolating the fluorescent signal. A smartphone camera (Samsung Galaxy S20 FE 5G; Samsung Electronics America, Inc., NJ, USA) was used to image bacterial droplets on surfaces. Any surface that was used to image was thoroughly cleaned with ethanol directly prior to imaging to ensure that there were not any outside sources contributing to the autofluorescent signals obtained. In order to simulate a real-life bacterial contamination, the droplets were placed on microscope slides or laboratory desks, and left to dry for 1-1.5 hours, after all the solvents were evaporated. The “pro” mode of the smartphone camera was used in taking images which allowed for the manual control: white balance = 2300K, ISO = 200, shutter speed = 2 s. The smartphone was placed 10 cm above the droplets, perpendicularly. Initially, the use of the smartphone flashlight and another bandpass filter was proposed but was not chosen due to a low signal intensity at 405 nm. A 9-V battery was used to power the 405 nm LED, which was held 20 cm away from the droplets to minimize light reflectance (Fig. 1). The optimal distances of the smartphone and the LED from the droplet were chosen by the process of trial and error to ensure the images obtained were not under or over saturated.

Each bacteria species was diluted 10-fold three times to obtain concentrations of each species from 10^7 CFU/mL to 10^4 CFU/mL, or the equivalent surface level concentrations of 10^5 to 10^3 CFU/cm². These were the final concentrations used for imaging. For laboratory desk experiments, a black laboratory desk surface was cleaned with ethanol right before each imaging

session. Then, six 20 μL droplets of each bacteria dilutions were placed onto the clean desk surface and allowed to dry for approximately 1-1.5 hr, depending on when the droplets become fully dry. After the droplets were dry, images were taken by a smartphone with the acrylic film and the 405 nm LED irradiating from the side (Fig. 1).

We also used a commercial UV flashlight (Vansky UV Flashlight; purchased from Amazon) with a total of 51 395 nm LEDs for comparison purposes. While it is designed to detect pet urine and bugs, it may also induce autofluorescence to bacteria, although the manufacturer did not advertise such capability. An identical imaging procedure was used. The removal of the acrylic film ensures the duplication of the intended usage of this UV flashlight since this device would typically be used to detect stains to the naked eye. Due to the high intensity of the UV flashlight, it was placed 50 cm away from the droplets, and images were taken.

Experiments without LB

While LB has been used to culture bacterial samples, LB cannot be found in practical samples. In addition, it is known that LB itself exhibits autofluorescence, albeit not intensely. Therefore, after completing the experiments with the LB-cultured bacteria samples on microscope slides, additional experiments were performed with the bacteria samples whose LB was removed. 500 μL of each bacteria species in the growth media was removed and placed into a clear 2-mL centrifuge tube. Each species was spun in the microcentrifuge (Galaxy 16D; VWR, Radnor, PA, USA) at 6000 RPM for 8 min. The supernatant of each tube was removed, around 495 μL , and then the same amount (495 μL) of DI water was added and used to resuspend each bacteria pellet. The concentration of each species was then determined using the same steps as described previously.

Image analysis

ImageJ (US National Institutes of Health; Bethesda, MD, USA) was used to process and analyze the images taken by the smartphone. Images were first cropped to isolate the droplet and then were split into blue, green, and red channels. Since the expected autofluorescence was in the green wavelength range, only the green channel was used to analyze the images, as shown in Fig. 2. ImageJ generated the pixel intensities (ranging from 0 to 255; 8-bit) for all pixels, and provided the number of pixels (x_i) at specific pixel intensity (i), e.g., 20 pixels showing the intensity of 100, 30 pixels showing the intensity of 101, etc. The following equation calculated the average intensity, where the denominator represents the total number of pixels, and the numerator represents all pixel intensities summed up. As shown in the equation, pixel intensities < 10 were not counted.

$$\text{Average intensity} = \frac{\sum_{i=10}^{255} (i * x_i)}{\sum_{i=10}^{255} x_i}$$

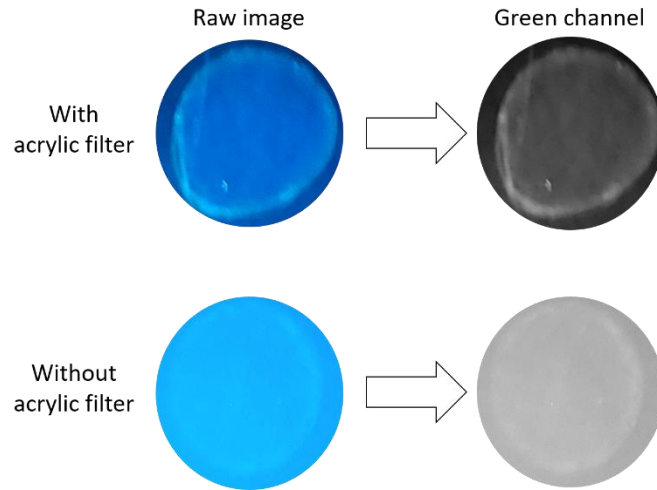


Figure B-2: Smartphone images (raw and green channel) of the bacteria droplets with vs. without an acrylic filter. Clearer fluorescence can be observed with an acrylic filter.

Results and discussion

Bacteria species with LB imaged on microscope slides

Three different species of bacteria in LB were used for this experiment: *E. coli*, *S. Typhimurium*, and *S. aureus*. Each species was diluted from 10^6 CFU/cm² (stock concentration) to 10^3 CFU/cm² and 6 droplets of each bacterial species at each concentration were placed on a microscope slide. The average intensity of each droplet was plotted against bacterial concentrations, as shown in Fig. 3. A diluted LB was the negative control for this experiment; LB was diluted in DI water. A linear decreasing trend was observed for the gram-positive bacteria, *S. aureus*, whereas the gram-negative bacteria, *E. coli* and *S. Typhimurium*, showed exponential decay. Nonetheless, all the bacterial species had a greater average intensity than the negative control, and it was confirmed that the autofluorescence was due to the presence of bacteria. The limit of detection (LOD) was 10^3 CFU/cm². Lower concentrations (not shown here) did not show significant differences from NC.

When the bacteria solution is diluted with DI water, the droplets form a ring-shaped structure (Fig. 3 on the top) due to the hydrophobicity of bacteria. The bacteria move towards the droplet's edges (three-phase borderline or contact line) to minimize their interactions with water molecules. Bacterial adhesion and droplet contact angle with the surface have previously demonstrated a strong correlation, which explains the hydrophobic interactions which drive DI-suspended bacteria to maintain as much self-contact as possible [23]. Prior research has shown that *E. coli* and *S. Typhimurium* are more hydrophobic than *S. aureus* [24], [25]. Greater hydrophobicity in bacterial species *E. coli* and *S. Typhimurium* can be attributed to their gram-negative cell walls compared to *S. aureus* which is gram positive [26]. Whereas gram positive cell walls are characterized by one thick peptidoglycan wall, gram negative bacteria possess an

additional second outer membrane made of particularly hydrophobic lipopolysaccharides. This difference in hydrophobicity, explains the exponential decay in *E. coli* and *S. Typhimurium* average intensities. High-level accumulation of such hydrophobic bacteria at the droplet's edges upon dilution would greatly diminish the intensity from the overall droplet. Although *S. aureus* also hydrophobic, the fluorescence signal is more spread out upon dilution, causing a more linear decrease in average intensity.

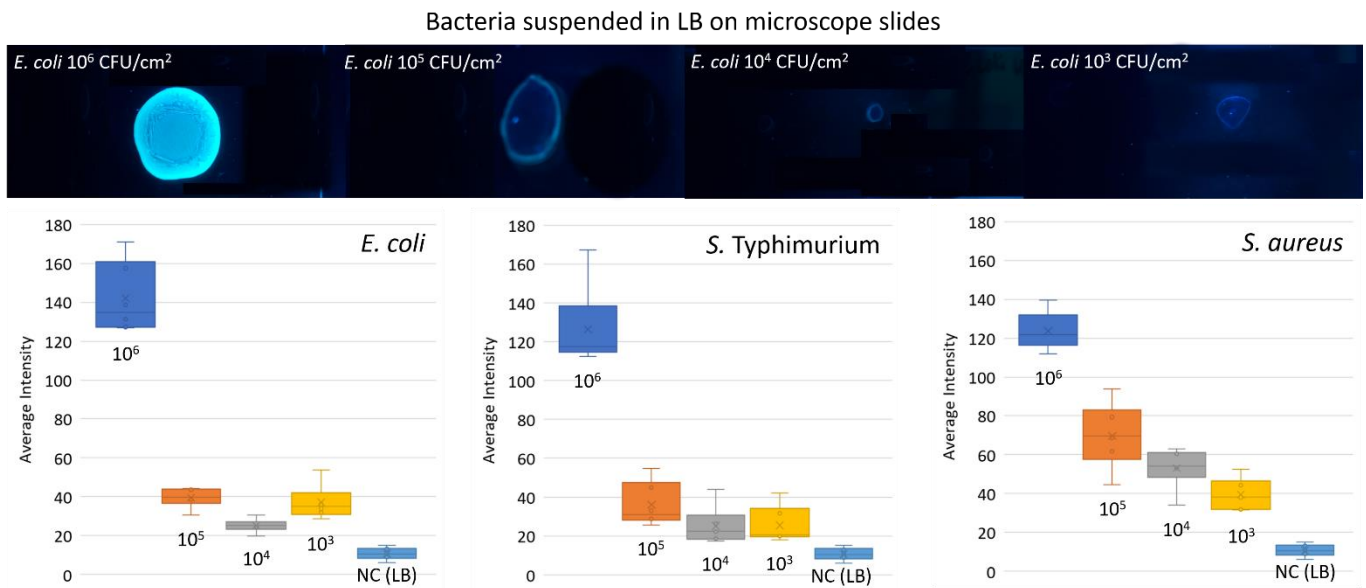


Figure B-3. Box and whisker plots of average intensities for bacteria droplets (suspended in LB and diluted in DI water) placed on microscope slides. Example images of *E. coli* droplets at various concentrations are shown in the top. Bottom shows the box and whisker plots of *E. coli*, *S. Typhimurium*, and *S. aureus* droplets at various concentrations (all in CFU/cm²). Negative control (NC) on each plot is a dilution of three orders of magnitude of LB.

Bacteria species with LB imaged on laboratory desks

Bacterial droplets were placed on a laboratory desk to represent a practical laboratory spillage. Similar trends were observed, and the LOD was again 10^3 CFU/cm² (Fig. 4). A black laboratory desk was chosen as it is standard in most laboratories. It also decreased the light reflection that might influence the average intensity. Microscope slide (glass) and laboratory desk (wood) are both hydrophilic surfaces, which causes the diluted bacteria to spread more with low contact angles, which is ideal for autofluorescence imaging. Bacterial concentrations did not significantly vary the droplet sizes. Since there was an overlap between the negative control and 10^3 CFU/cm² bacteria, in the next set of experiments, LB was removed from the solution to eliminate fluorescent signals from LB.

Bacteria suspended in LB on laboratory desks

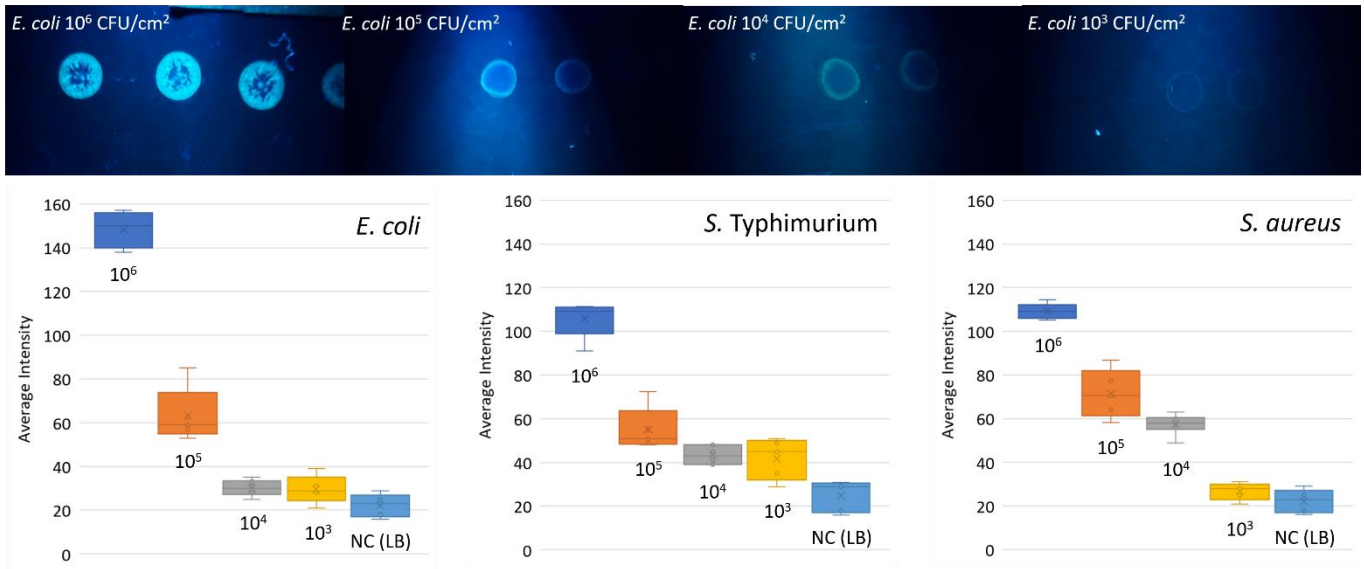


Figure B-4. Box and whisker plots of average intensities for bacteria droplets (suspended in LB and diluted in DI water) placed on laboratory desks. Example images of *E. coli* droplets at various concentrations are shown in the top. Bottom shows the box and whisker plots of *E. coli*, *S. Typhimurium*, and *S. aureus* droplets at various concentrations (all in CFU/cm²). Negative control (NC) on each plot is a dilution of three orders of magnitude of LB.

Selection of controls

One of the main goals of this work was to observe surface contaminants in a laboratory environment. Therefore, several solutions that could be found in a laboratory setting were chosen as controls. Tap water was selected as it is commonly found on laboratory surfaces, typically around the sink area. Salt solution was chosen as another control due to its possibility of being found on a laboratory surface. In addition, proteins, specifically bovine serum albumin (BSA) that are commonly used in biological laboratories, would offer an excellent comparison to bacteria. BSA also emits fluorescence signals at 550 nm when excited with a 380 nm light source [27]. The autofluorescence of BSA can be attributed to its two tryptophan residues: Trp-134 and Trp-212 which both demonstrate intrinsic fluorescence [27]. Finally, since each bacteria species was suspended in LB or resuspended in DI water, both were also used as controls depending on the experiments.

Bacteria species resuspended in DI water imaged on laboratory desk

The same three species of bacteria, *E. coli*, *S. Typhimurium*, and *S. aureus*, were used in this set of experiments. The main difference in these experiments is the removal of LB from the bacteria samples. In the previous set of experiments it was determined that some of the autofluorescent signals were coming from the presence of LB. Due to this, experiments were run to test the autofluorescence intensity of serially diluted LB (Supplementary Fig. 1). To remove any interference from the culture media the presence of LB was removed according to the experiments without LB section in order to ensure that no autofluorescent signal was coming from LB. In order to ensure that the resuspended bacteria were still alive, a 10^7 CFU/cm² sample of each resuspended (in DI water) bacterial species were plated on a LB agar plate and left in the

incubator overnight. As a control, a 10^7 CFU/cm² concentration of each bacterial species suspended in LB were plated on a LB agar plate and incubated overnight as well. The colonies formed in both the control and the resuspended bacteria were similar, therefore the bacteria detected on the laboratory desk were still alive and the results in fig. 5 were not affected. This removal ensured that none of the signals was coming from LB. In addition, various control samples were also tested, as explained in the previous section. Fig. 5 represents the average intensity values of each bacteria species, *E. coli*, *S. Typhimurium*, and *S. aureus*, at concentrations of 10^5 , 10^4 , and 10^3 CFU/cm² for each species. In this set of experiments, 10^6 CFU/cm² concentration was not tested since the LB removal decreased the stock concentration to 10^7 CFU/mL (= 10^5 CFU/cm²). The average intensity value of each bacteria species at 10^5 CFU/cm² was higher than its counterpart at 10^4 CFU/cm². This decrease in the average autofluorescence intensity is analogous to the results shown in Fig. 4. Finally, images were taken for each bacterial species at 10^3 CFU/cm²; however, no signal was detected (zero intensities). The intensity of DI water was also zero since there was no LB contributing to the autofluorescence. This leads the LOD to be 10^4 CFU/cm². The traditional method of swabbing a surface typically would have a LOD of 10^4 CFU/mL which would be equivalent to 10^2 CFU/cm² for a surface concentration [28]. Although a lower limit of detection would be more ideal, the observed limit of detection was able to be detected with a low-cost, time effective, and simple device. Fig. 5 also includes the average intensity values of each of the controls. The controls of NaCl (model salt) and BSA (model protein) were made at 1 μ g/mL, representing the surface concentration of 10 mg/cm². This concentration is equivalent to the LOD of 10^4 CFU/cm² (= 10^6 CFU/mL), since 1 CFU bacteria was approximated to be 1 pg. This conversion was made based on the standard dry mass of an E. Coli cell, 1 pg, assuming that one cell will form 1 CFU [29].

Tap water was also used; according to the local water supplier, its chlorine level is regulated from 0.8 to 1.2 ppm (= 0.8 to 1.2 $\mu\text{g}/\text{mL}$). Again, this chlorine concentration is equivalent to 8-12 mg/cm^2 . The presence of chlorine in the tap water is hypothesized to create some autofluorescent signal which can also be observed in fig. 5 and fig. 6 [30]. As mentioned earlier, BSA contains tryptophan which is responsible for the fluorescent signal observed in fig. 5. However, since porphyrins are optimally excited at 405nm, the bacterial species emits a higher fluorescent signal. The average intensity for each control is lower than the average intensity values for the $10^5 \text{ CFU}/\text{cm}^2$ and $10^4 \text{ CFU}/\text{cm}^2$ concentrations. This result demonstrates a difference in the average autofluorescence intensities between bacterial species and non-microbial controls.

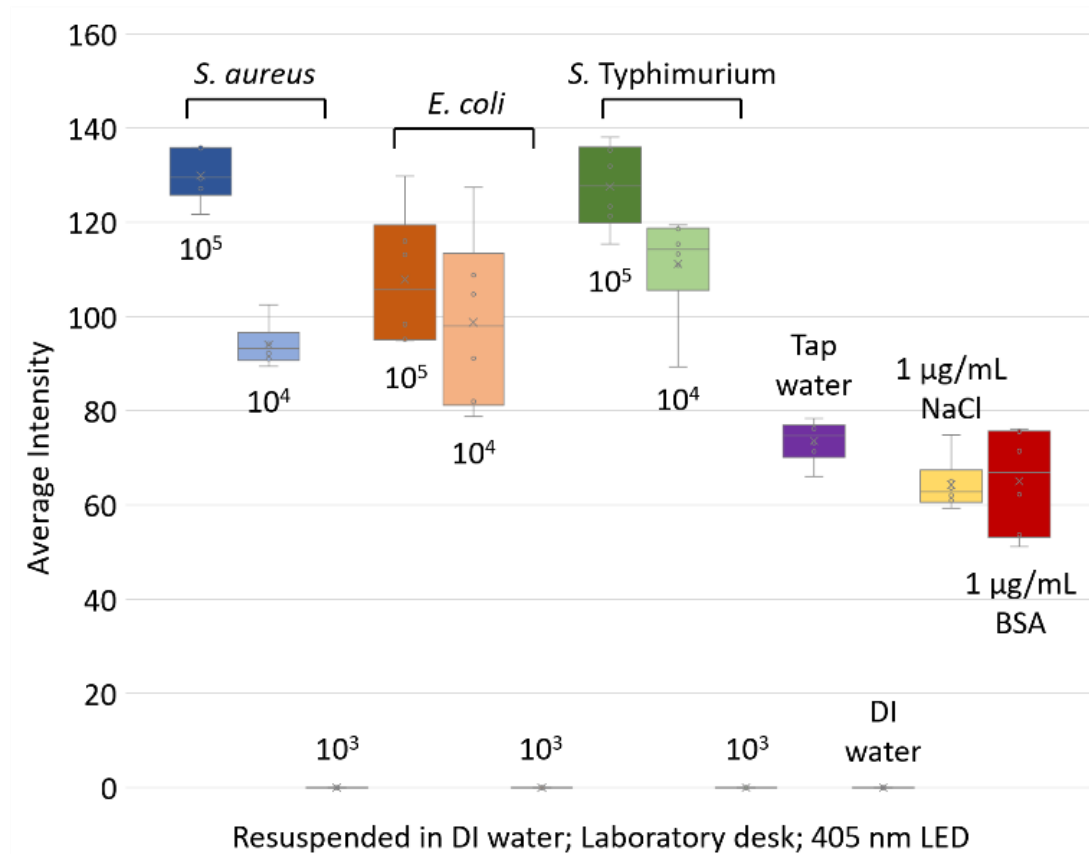


Figure B-5. Box and whisker plot of the average intensities of each bacteria species, *E. coli*, *S. Typhimurium*, and *S. aureus*, at the concentrations of 10^5 , 10^4 , and 10^3 CFU/cm². LB was removed from bacterial samples. A smartphone, a 405 nm LED, an acrylic film, and green channel images were used. The controls of tap water (0.8-1.2 ppm), DI water, NaCl solution (1 µg/mL), and BSA solution (1 µg/mL) are also plotted. These control concentrations are equivalent to 10 mg/cm², approximating the LOD of bacteria, 10^4 CFU/cm².

Experiments with a commercial UV flashlight

A UV flashlight was purchased and used to image each bacteria species, *E. coli*, *S. Typhimurium*, and *S. aureus*, from 10^5 through 10^3 CFU/cm² and each of the controls mentioned in the previous section. Fig. 6 displays the average intensity values obtained for each bacteria species and controls. Since the excitation was UV at 395 nm, the blue channel was analyzed instead of the green channel [30]–[32]. In addition, the commercial UV flashlight provided a higher light intensity compared to the 405 nm LED. Therefore, the UV flashlight was placed further away from the droplets as described in materials and methods in order to not over saturate the fluorescence signal. The UV flashlight could not detect any of the bacteria species at a concentration of 10^4 CFU/cm² and below, leading to the zero values that appear in Fig. 6. Although the wavelength of the flashlight was similar to our system's light source, the high number of LEDs in the flashlight and its distance from the droplet prevents it from exciting the droplet as precisely as the single 405nm LED in our system. While the bacterial samples at 10^5 CFU/cm² showed strong blue intensities, all three control samples – tap water, NaCl solution, and BSA solution – also showed strong blue signals, which rendered this method unable to identify bacterial presence on laboratory desk surfaces.

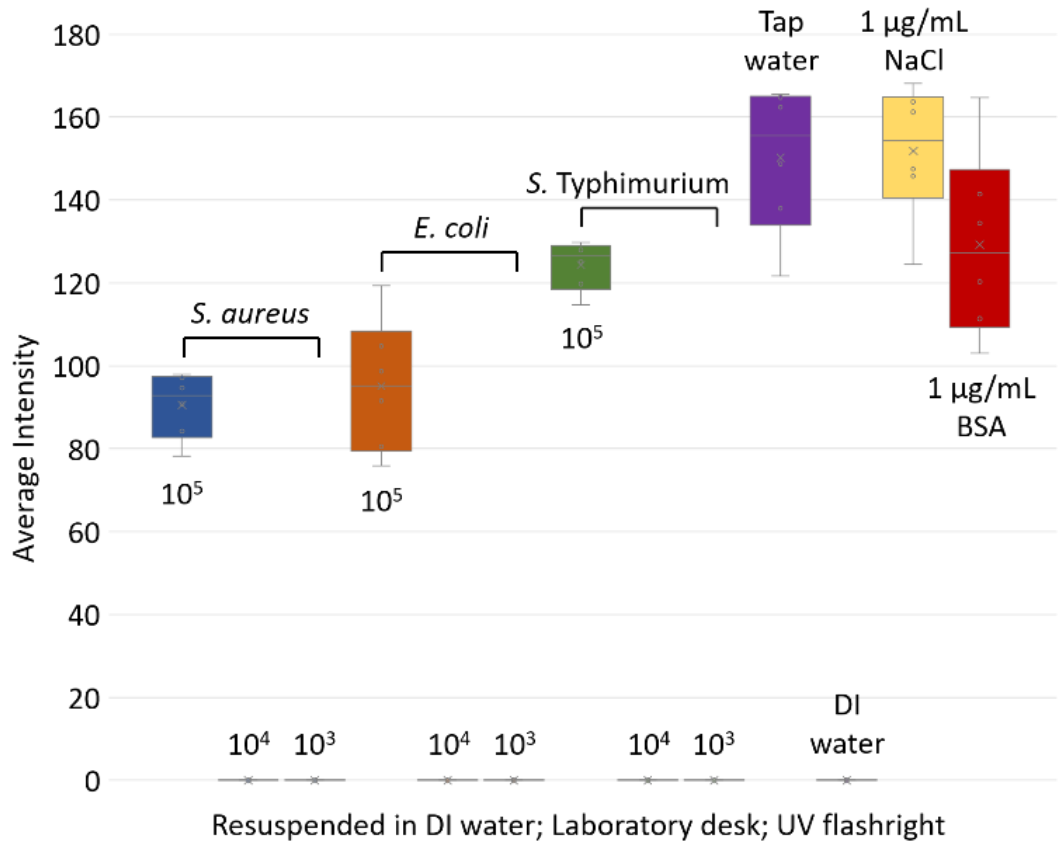


Figure B-6. Experiments were repeated with a commercial UV flashlight instead of a 405 nm LED. Blue channel images were used. All other conditions are identical to those shown in Fig. 5.

Conclusions

Bacteria contaminations in biological and clinical laboratory settings are common due to the nature of the research or hospital-wide microbial infection. However, there are no known methods to effectively detect bacteria on laboratory surfaces using autofluorescence signals. In this work, a smartphone platform was implemented to create an imaging setup that could image autofluorescence signals emitting from various bacteria species (*E. coli*, *S. Typhimurium*, and *S. aureus*) and controls (tap water, salt solution, and protein solution). Only a low-cost acrylic film and an LED were necessary, in addition to a smartphone. The images were processed through ImageJ to obtain average intensity values that could be compared against each other. When comparing bacteria species and controls, in the imaging setup, the bacterial species exhibited an overall higher average intensity value than the controls test. The limit of detection was 10^4 CFU/cm². Whereas the UV flashlight was unable to differentiate between bacteria and controls making the imaging setup a superior method. This preliminary work highlights the ability of cost-effective materials, such as a smartphone platform, a 405 nm LED, and an acrylic film, to image potential laboratory surface contaminants. Future work should include the development of a smartphone application that allows for analyzing images and detecting bacterial presence directly from the smartphone.

Acknowledgements

This work was supported by the University of Arizona's Test All Test Smart program and the Arizona Board of Regent's Technology and Research Initiative Fund (TRIF). We thank Dr. Sangsik Kim for their help with bacteria culture.

References

- [1] “Contamination in a Microbiological Laboratory,” *International Journal of Research Studies in Biosciences*, vol. 6, no. 4, 2018, doi: 10.20431/2349-0365.0604002.
- [2] L. S. Y. Ng, W. T. Teh, S. K. Ng, L. C. Eng, and T. Y. Tan, “Bacterial contamination of hands and the environment in a microbiology laboratory,” *Journal of Hospital Infection*, vol. 78, no. 3, pp. 231–233, Jul. 2011, doi: 10.1016/j.jhin.2011.01.025.
- [3] R. Kosif and F. Avcioglu, “An Examination of Bacterial Contamination of Models Used in Anatomy Laboratories,” *Interdisciplinary Perspectives on Infectious Diseases*, vol. 2018, pp. 1–5, Dec. 2018, doi: 10.1155/2018/9201312.
- [4] M. Schmidlin, M. Alt, G. Vogel, U. Voegeli, P. Brodmann, and C. Bagutti, “Contaminations of laboratory surfaces with *Staphylococcus aureus* are affected by the carrier status of laboratory staff,” *Journal of Applied Microbiology*, vol. 109, no. 4, pp. 1284–1293, Oct. 2010, doi: 10.1111/j.1365-2672.2010.04749.x.
- [5] R. M. Goulter, I. R. Gentle, and G. A. Dykes, “Issues in determining factors influencing bacterial attachment: a review using the attachment of *Escherichia coli* to abiotic surfaces as an example,” *Letters in Applied Microbiology*, vol. 49, no. 1, pp. 1–7, Jul. 2009, doi: 10.1111/j.1472-765X.2009.02591.x.
- [6] R. E. Sweeney, E. Budiman, and J.-Y. Yoon, “Mie scatter spectra-based device for instant, contact-free, and specific diagnosis of bacterial skin infection,” *Scientific Reports*, vol. 7, no. 1, p. 4801, Dec. 2017, doi: 10.1038/s41598-017-05061-1.

- [7] S. v. Angus, S. Cho, D. K. Harshman, J.-Y. Song, and J.-Y. Yoon, “A portable, shock-proof, surface-heated droplet PCR system for *Escherichia coli* detection,” *Biosensors and Bioelectronics*, vol. 74, pp. 360–368, Dec. 2015, doi: 10.1016/j.bios.2015.06.026.
- [8] K. E. McCracken, S. v. Angus, K. A. Reynolds, and J.-Y. Yoon, “Multimodal Imaging and Lighting Bias Correction for Improved μ PAD-based Water Quality Monitoring via Smartphones,” *Scientific Reports*, vol. 6, no. 1, p. 27529, Jun. 2016, doi: 10.1038/srep27529.
- [9] J.-Y. Yoon, “Smartphone based medical diagnostics,” 2020.
- [10] M. Rennie, D. Dunham, L. Lindvere-Teene, R. Raizman, R. Hill, and R. Linden, “Understanding Real-Time Fluorescence Signals from Bacteria and Wound Tissues Observed with the MolecuLight i:XTM,” *Diagnostics*, vol. 9, no. 1, p. 22, Feb. 2019, doi: 10.3390/diagnostics9010022.
- [11] J. Surre, C. Saint-Ruf, V. Collin, S. Orenge, M. Ramjeet, and I. Matic, “Strong increase in the autofluorescence of cells signals struggle for survival,” *Scientific Reports*, vol. 8, no. 1, p. 12088, Dec. 2018, doi: 10.1038/s41598-018-30623-2.
- [12] L. Yang, Y. Zhou, S. Zhu, T. Huang, L. Wu, and X. Yan, “Detection and Quantification of Bacterial Autofluorescence at the Single-Cell Level by a Laboratory-Built High-Sensitivity Flow Cytometer,” *Analytical Chemistry*, vol. 84, no. 3, pp. 1526–1532, Feb. 2012, doi: 10.1021/ac2031332.
- [13] S. Patiño *et al.*, “Autofluorescence of mycobacteria as a tool for detection of *Mycobacterium tuberculosis*,” *J Clin Microbiol*, vol. 46, no. 10, pp. 3296–302, Oct. 2008, doi: 10.1128/JCM.02183-07.

- [14] M. S. Ammor, “Recent Advances in the Use of Intrinsic Fluorescence for Bacterial Identification and Characterization,” *Journal of Fluorescence*, vol. 17, no. 5, pp. 455–459, Sep. 2007, doi: 10.1007/s10895-007-0180-6.
- [15] L. Leblanc, “Monitoring the identity of bacteria using their intrinsic fluorescence,” *FEMS Microbiology Letters*, vol. 211, no. 2, pp. 147–153, Jun. 2002, doi: 10.1016/S0378-1097(02)00636-5.
- [16] A. Sivaraman *et al.*, “A Novel, Smartphone-Based, Teleophthalmology-Enabled, Widefield Fundus Imaging Device With an Autocapture Algorithm,” *Translational Vision Science & Technology*, vol. 10, no. 12, p. 21, Oct. 2021, doi: 10.1167/tvst.10.12.21.
- [17] P. Kheamphet and P. Masawat, “A simple and cost-effective smartphone-based digital imaging device for the quantification of selected heavy metals in Thai rice,” *Analytical Methods*, vol. 14, no. 2, pp. 165–173, 2022, doi: 10.1039/D1AY01816G.
- [18] M. Rennie, D. Dunham, L. Lindvere-Teene, R. Raizman, R. Hill, and R. Linden, “Understanding Real-Time Fluorescence Signals from Bacteria and Wound Tissues Observed with the MolecuLight i:XTM,” *Diagnostics*, vol. 9, no. 1, p. 22, Feb. 2019, doi: 10.3390/diagnostics9010022.
- [19] S. Kang, E. Josselin de Jong, S. M. Higham, C. K. Hope, and B. Kim, “Fluorescence fingerprints of oral bacteria,” *Journal of Biophotonics*, vol. 13, no. 1, Jan. 2020, doi: 10.1002/jbio.201900190.
- [20] J. S. Dickson and M. Koohmaraie, “Cell surface charge characteristics and their relationship to bacterial attachment to meat surfaces,” *Applied and Environmental*

- Microbiology*, vol. 55, no. 4, pp. 832–836, Apr. 1989, doi: 10.1128/aem.55.4.832-836.1989.
- [21] M. Shu *et al.*, “Porphyrin Metabolisms in Human Skin Commensal Propionibacterium acnes Bacteria: Potential Application to Monitor Human Radiation Risk,” *Current Medicinal Chemistry*, vol. 20, no. 4, pp. 562–568, Jan. 2013, doi: 10.2174/0929867311320040007.
- [22] J. Fyrestam, N. Bjurshammar, E. Paulsson, A. Johannsen, and C. Östman, “Determination of porphyrins in oral bacteria by liquid chromatography electrospray ionization tandem mass spectrometry,” *Analytical and Bioanalytical Chemistry*, vol. 407, no. 23, pp. 7013–7023, Sep. 2015, doi: 10.1007/s00216-015-8864-2.
- [23] M. C. van Loosdrecht, J. Lyklema, W. Norde, G. Schraa, and A. J. Zehnder, “The role of bacterial cell wall hydrophobicity in adhesion,” *Applied and Environmental Microbiology*, vol. 53, no. 8, pp. 1893–1897, Aug. 1987, doi: 10.1128/aem.53.8.1893-1897.1987.
- [24] S. Kim, A. Romero-Lozano, D. S. Hwang, and J.-Y. Yoon, “A guanidinium-rich polymer as a new universal bioreceptor for multiplex detection of bacteria from environmental samples,” *Journal of Hazardous Materials*, vol. 413, p. 125338, Jul. 2021, doi: 10.1016/j.jhazmat.2021.125338.
- [25] X. Ma *et al.*, “A Biocompatible and Biodegradable Protein Hydrogel with Green and Red Autofluorescence: Preparation, Characterization and In Vivo Biodegradation Tracking and Modeling,” *Scientific Reports*, vol. 6, no. 1, p. 19370, May 2016, doi: 10.1038/srep19370.
- [26] A. Ebbensgaard, H. Mordhorst, F. M. Aarestrup, and E. B. Hansen, “The Role of Outer Membrane Proteins and Lipopolysaccharides for the Sensitivity of Escherichia coli to

- Antimicrobial Peptides,” *Frontiers in Microbiology*, vol. 9, Sep. 2018, doi: 10.3389/fmicb.2018.02153.
- [27] M. Tan, W. Liang, X. Luo, and Y. Gu, “Fluorescence Spectroscopy Study on the Interaction between Evodiamine and Bovine Serum Albumin,” *Journal of Chemistry*, vol. 2013, pp. 1–6, 2013, doi: 10.1155/2013/308054.
- [28] C. Griffith, “Surface Sampling and the Detection of Contamination,” in *Handbook of Hygiene Control in the Food Industry*, Elsevier, 2016, pp. 673–696. doi: 10.1016/B978-0-08-100155-4.00044-3.
- [29] A. C. Guo *et al.*, “ECMDB: The E. coli Metabolome Database,” *Nucleic Acids Research*, vol. 41, no. D1, pp. D625–D630, Oct. 2012, doi: 10.1093/nar/gks992.
- [30] J. Y. Yoon, “Introduction to Biosensors: From Electric Circuits to Immunosensors: Second edition,” *Introduction to Biosensors: From Electric Circuits to Immunosensors: Second Edition*, pp. 1–331, Jan. 2016, doi: 10.1007/978-3-319-27413-3.
- [31] K. Xiao *et al.*, “Stokes Shift and Specific Fluorescence as Potential Indicators of Organic Matter Hydrophobicity and Molecular Weight in Membrane Bioreactors,” *Environmental Science & Technology*, vol. 53, no. 15, pp. 8985–8993, Aug. 2019, doi: 10.1021/acs.est.9b02114.
- [32] H. R. Petty, V. M. Elner, T. Kawaji, A. Clark, D. Thompson, and D.-L. Yang, “A facile method for immunofluorescence microscopy of highly autofluorescent human retinal sections using nanoparticles with large Stokes shifts,” *Journal of Neuroscience Methods*, vol. 191, no. 2, pp. 222–226, Aug. 2010, doi: 10.1016/j.jneumeth.2010.07.001.